

## A stabilized iterative scheme for coupled hydro-mechanical systems using reproducing kernel particle method

Yongning Xie and Gang Wang<sup>\*,†</sup>

*Department of Civil and Environmental Engineering, The Hong Kong University of Science and Technology, Clear Water Bay, Kowloon, Hong Kong*

### SUMMARY

In this paper, a novel iterative coupling scheme is developed for solving coupled hydro-mechanical problems using reproducing kernel particle method. The numerical scheme calls the fluid and the solid solvers sequentially and iteratively until convergent solutions are obtained. To overcome the numerical instability problem, a simple stabilization technique is developed and proved to be unconditionally stable through stability analysis. The accuracy and convergence of the proposed numerical scheme are demonstrated through extensive parametric studies of one-dimensional and two-dimensional consolidation simulations using fully saturated elastic medium as well as biaxial test using a fully nonlinear soil model. Copyright © 2014 John Wiley & Sons, Ltd.

Received 25 September 2013; Revised 14 March 2014; Accepted 5 May 2014

KEY WORDS: hydro-mechanical coupling; iterative; meshfree; numerical stability

### 1. INTRODUCTION

Simulating coupling phenomenon of fluid in porous solid medium has found many important applications in the design of geotechnical structures, reservoir engineering, and oil industry. However, developing an accurate and stable numerical scheme to solve the coupled hydro-mechanical systems is always a great challenge. During the past 30 years, finite element method (FEM) has been widely used to solve the coupled systems. One may refer to [1] for a comprehensive exposition of the mathematical theories and numerical algorithms. As an alternative approach, the meshfree method is free from element construction and was extensively developed in the past decade. There have been a few attempts to apply the meshfree method to solve the coupled hydro-mechanical problems. In general, the meshfree method is advantageous over the standard FEM in producing more accurate and smoother solutions for coupling problems due to the high-order interpolation used [2, 3]. A variety of other techniques of using meshfree methods to solve the coupled hydro-mechanical problems have also been explored, for example, in terms of meshfree spatial discretization, solution strategies, the constitutive models implemented and specifics of the problems under study.

For meshfree spatial discretization, most of the past studies employed element free Galerkin method [3–7] and point interpolation method or radial point interpolation method [8–11]. Smooth particle hydrodynamics is also used occasionally [12]. The displacement of porous solid skeleton and pore fluid pressure can also be approximated using different interpolation schemes. For example, the displacements in the solid skeleton are represented by standard FEM nodes, while the pore fluid pressure is interpolated using element free Galerkin method nodes in [2]. On the other hand,

---

\*Correspondence to: Gang Wang, Department of Civil and Environmental Engineering, The Hong Kong University of Science and Technology, Clear Water Bay, Kowloon, Hong Kong.

†E-mail: gwang@ust.hk

reproducing kernel particle method (RKPM) was first employed by [13] as an effective numerical homogenization method to calculate strain localizations in the particulate medium. The nonlocal RKPM is found to be capable of smoothing the erratic displacements in strain localizations. Extensive application of RKPM in shear band simulations of inelastic materials has demonstrated the clear advantages of RKPM in alleviating mesh-alignment sensitivity, in capturing high-resolution shear bands, and in providing a favorable condition for hp-adaptivity and so on [14–17]. However, RKPM has not yet been applied for solving coupled hydro-mechanical problems.

The solution strategies for solving the coupled fluid and solid system also vary. In most cases, the primary unknowns are the displacements of the solid skeleton and pore fluid pressure. The primary unknowns can be solved simultaneously using a global system of equations, and the scheme is referred to as *fully coupled scheme* in this paper. Although it appears to be straightforward, the global matrix of the fully coupled system may be ill-conditioned because of distinct properties and behaviors between the solid and the fluid. Moreover, the global matrix may become singular if the fluid is incompressible and the solid–fluid mixture is impermeable, resulting in nonphysical oscillation of the distribution of the pore fluid pressure [4]. Under the condition of incompressible and impermeable limit, it is often required that a reduced order of interpolation should be adopted for the pore fluid pressure to stabilize the solutions. Alternatively, stabilization techniques can be used to regulate the governing equations. For example, [18] stabilized the system by introducing a stabilization term consisting of the spatial derivatives of pore pressure to the governing equations. Reference [4] proposed a stabilization scheme by rearranging the system matrix and taking advantage of meshfree nodal distribution.

Iterative coupling scheme is another promising strategy to solve the coupled hydro-mechanical systems (e.g., [9, 19, 20]). It has significant advantage over the fully coupled scheme due to its *modularity* such that the fluid and the mechanical solver for corresponding governing equations can be executed separately without many extra manipulations, which is particularly desirable in many practical applications. The coupling effects are reinforced through the information exchange between the solid and fluid solvers (note that more solvers may be involved depending on the specific problems). However, numerical stability and efficiency are outstanding problems that are frequently encountered using the iterative schemes. Reference [21] conducted a detailed convergence analysis of the block Gauss–Seidel method, which is an iterative method widely used for strongly coupled fluid-structure systems. Different convergence behaviors may be experienced with different time integration schemes, relaxation parameters, and degrees of nonlinearities. To improve numerical efficiency, [22] derived error bounds for the block Gauss–Seidel method and used them as indicators to terminate numerical iterations. Other iterative solution strategies also show varied stability performance for coupled multifield problems [23] and coupled flow problems [24, 25]. Special techniques are often needed to accelerate the rate of convergence during the iterations to reduce the computational cost [9].

To date, most of the constitutive models employed in the coupled hydro-mechanical analysis are simple linearly elastic materials for solids. Numerical solutions are usually verified using a few examples, such as one-dimensional or two-dimensional consolidation and water pumping, as the analytical solutions are available for these special cases [3, 7]. In a few studies, elasto-plastic solids are used to simulate the strain localization [26]. Parametric studies have also been conducted. For example, [3] and [27] investigated the effects of time step, penalty factor, size of influence domain, number of Gauss points, and type of weight functions on the numerical results. Guidelines for appropriately choosing these parameters are proposed. Other interesting aspects include model dimensions from 1D to 2D and to 3D [7], loading modes from quasi-static to dynamic loading [9, 28], as well as anisotropy of hydraulic properties [4], just to name a few.

In this study, a stable iterative coupling scheme is developed using RKPM. A distinct feature of the proposed numerical scheme is that the displacement of porous solid  $\mathbf{u}$  and pore fluid pressure  $p$  share the same set of nodes and shape functions, that is, equal order of interpolation for  $\mathbf{u}$  and  $p$ . The numerical scheme calls the fluid and the solid solvers sequentially and iteratively until convergent solutions are obtained. A stabilization technique is introduced, and the numerical scheme is proved to be unconditionally stable using an appropriate relaxation parameter.

This paper is arranged as follows: governing equations for the hydro-mechanical system are presented in Section 2. In Section 3, the RKPM is briefly introduced, together with a transformation method to reinforce the essential boundary conditions. The spatial and temporal discretizations of the governing equations are then presented using RKPM. The detailed algorithm for the iterative coupling scheme is presented in Section 4, followed by stability analysis of the numerical scheme in Section 5. Finally, verification and application of the proposed scheme are demonstrated in Section 6 using one-dimensional and two-dimensional consolidation of fully saturated linearly elastic ground. Biaxial test of nonlinear soil sample is also conducted. Parametric studies on convergence rate of the algorithm and treatment of the incompressible and impermeable limit are also presented.

Throughout the paper, letters in bold face denote tensors or vectors. A subscript  $j$  following a comma as in  $(\ )_{,j}$  denotes partial derivative with respect to coordinate  $x_j$ . A superimposed dot over a variable  $(\dot{\ })$  denotes the time derivative of that variable.  $\delta_{ij}$  is the Kronecker delta tensor. Summation on repeated indices is implied unless stated otherwise. For sign convention, tension in the solid phase and compression in the fluid phase are considered to be positive.

## 2. GOVERNING EQUATIONS OF THE COUPLED HYDRO-MECHANICAL SYSTEM

In this study, the solid–fluid mixture is described using continuum mechanics. As shown in Figure 1, the solid–fluid mixture contains the solid phase and fluid phase in the voids. The assemblage of all solid particles form the solid skeleton. The  $\mathbf{u} - p$  formulation is adopted to formulate the governing equations for the coupled systems [1]. The displacement of the solid skeleton,  $\mathbf{u}$ , and the pore fluid pressure  $p$  are the primary unknowns.

First, the balance of the momentum of the solid–fluid mixture is written as follows:

$$\sigma_{ij,j} - \rho \ddot{u}_i + \rho b_i = 0 \quad (1)$$

where  $\sigma_{ij}$  is total stress tensor, which is related to the effective stress  $\sigma'_{ij}$  and pore fluid pressure  $p$  via Terzaghi's effective stress concept, that is,  $\sigma_{ij} = \sigma'_{ij} - p\delta_{ij}$ .  $\rho$  is the total density of the solid–fluid mixture. If the solid is fully saturated,  $\rho = n\rho_f + (1 - n)\rho_s$ , where  $n$  is porosity,  $\rho_f$  and  $\rho_s$  are densities of fluid and solid, respectively.  $b_i$  is the unit body force in the  $i$ th direction.

The second governing equation describes the conservation of fluid mass:

$$(k_{ij}(-p_{,j} + \rho_f b_j))_{,i} + \dot{u}_{i,i} + \frac{n\dot{p}}{K_f} = 0 \quad (2)$$

where  $K_f$  is the bulk modulus of the fluid.  $k_{ij}$  is the permeability tensor (in the unit of  $\text{m}^2/(\text{Pa} \cdot \text{sec})$ ). The tensorial formulation of the permeability makes it convenient to describe hydraulic anisotropy. If the permeability is isotropic,  $k_{ij}$  can be represented as a scalar  $k$ , which can be related to the

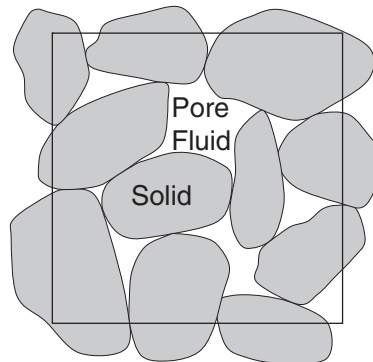


Figure 1. Schematic illustration of a representative volume element for the solid–fluid mixture.

hydraulic conductivity  $k_H$  (in m/sec) by  $k = \frac{k_H}{\gamma_w}$ , where  $\gamma_w$  is the specific weight of the fluid, or it can be related to the *intrinsic permeability*  $\kappa$  (in  $\text{m}^2$ ) via  $k = \frac{\kappa}{\mu}$ , where  $\mu$  is the dynamic viscosity (in  $\text{N} \cdot \text{sec}/\text{m}^2$ ). The permeability can be a function of the degree of saturation and void ratio, and so on. Nevertheless, constant permeability is used in this formulation unless otherwise stated. Also note that individual solid grains are assumed to be incompressible here.

The prescribed boundary conditions are

$$\begin{aligned} \sigma_{ij}n_j &= \bar{t}_i & \text{on } \Gamma_t \\ u_i &= \bar{u}_i & \text{on } \Gamma_u \\ p_i &= \bar{p}_i & \text{on } \Gamma_p \\ q = \bar{q} &= -n_i k_{ij}(-p_{,j} + \rho_f b_j) & \text{on } \Gamma_w \end{aligned} \tag{3}$$

where  $\Gamma_t, \Gamma_u, \Gamma_p, \Gamma_w$  are the traction boundary, displacement boundary, pressure boundary, and flux boundary, respectively. The total boundary  $\Gamma = \Gamma_t \cup \Gamma_u = \Gamma_p \cup \Gamma_w$  and  $\Gamma_t \cap \Gamma_u = \Gamma_p \cap \Gamma_w = \emptyset$  (empty set).  $\bar{t}_i, \bar{u}_i, \bar{p}_i$ , and  $\bar{q}$  are the prescribed traction, displacement, pressure, and influx on the boundaries.  $n_i$  is outward unit normal vector to the boundary (note that it should not be confused with the aforementioned porosity  $n$ ). Aside from the boundary conditions, initial conditions  $u = u_0, p = p_0$  should also be assigned for the numerical simulations at  $t = 0$ .

The constitutive behavior of the solid skeleton is controlled by the effective stress  $\sigma'_{ij}$ . A general rate form of the effective-stress-based constitutive model reads

$$\dot{\sigma}'_{ij} = C_{ijkl} \dot{\varepsilon}_{kl} \tag{4}$$

where  $C_{ijkl}$  is the tangent modulus of the solid skeleton,  $\varepsilon_{ij}$  is the small-strain tensor defined as  $\varepsilon_{ij} = \frac{1}{2}(u_{i,j} + u_{j,i})$ . The constitutive model can be linearly elastic or fully nonlinear. In the latter case, the tangent modulus may depend on the stress-strain state of the material.

As shown through the governing equations, the solid–fluid behaviors that are coupled in that changing pore pressure affect the mechanical equilibrium state of the mixture, while the volumetric strain rate of solid skeleton  $\dot{u}_{i,i}$  affects the mass balance of the fluid through volumetric strain, permeability, and porosity. For simplicity, permeability and porosity are assumed constants throughout the simulations unless otherwise stated. A successful numerical scheme should be able to solve the system considering the aforementioned coupling effect.

### 3. DISCRETIZATION OF GOVERNING EQUATIONS

In this section, the spatial and temporal discretization of the governing equations are presented using the RKPM. A transformation method is formulated to enforce the essential boundary conditions.

#### 3.1. RKPM spatial discretization

3.1.1. *RKPM interpolant.* Following the Moving Least Square Reproducing Kernel interpolant proposed by [29], a local approximation to  $u(\mathbf{x})$  can be written as:

$$u(\mathbf{x}) \cong u^h(\mathbf{x}) = L_{\bar{\mathbf{x}}} u(\mathbf{x}) := \mathbf{P}^T \left( \frac{\mathbf{x} - \bar{\mathbf{x}}}{\varrho} \right) \mathbf{a}(\bar{\mathbf{x}}) \tag{5}$$

where  $\mathbf{P}(\mathbf{x})$  is a basis with  $\mathbf{P}_1(\mathbf{x}) = 1$ ,  $\mathbf{a}(\bar{\mathbf{x}})$  are coefficients to be determined.

Define an error functional weighted by a scaled window function  $w_\rho(\mathbf{x} - \bar{\mathbf{x}})$  as follows:

$$J(\mathbf{a}(\bar{\mathbf{x}})) = \int_{\Omega} \left[ u(\mathbf{x}) - \mathbf{P}^T \left( \frac{\mathbf{x} - \bar{\mathbf{x}}}{\rho} \right) \mathbf{a}(\bar{\mathbf{x}}) \right]^2 w_\rho(\mathbf{x} - \bar{\mathbf{x}}) d\Omega \quad (6)$$

where

$$w_\rho(\mathbf{x} - \bar{\mathbf{x}}) = \frac{1}{\rho} \cdot w \left( \frac{\mathbf{x} - \bar{\mathbf{x}}}{\rho} \right) \quad (7)$$

Minimizing  $J(\mathbf{a}(\bar{\mathbf{x}}))$  with respect to  $\mathbf{a}(\bar{\mathbf{x}})$ , that is,  $\frac{\partial J(\mathbf{a}(\bar{\mathbf{x}}))}{\partial \mathbf{a}(\bar{\mathbf{x}})} = 0$ , one has

$$\left( \int_{\Omega_x} \mathbf{P} \left( \frac{\mathbf{x} - \bar{\mathbf{x}}}{\rho} \right) w_\rho(\mathbf{x} - \bar{\mathbf{x}}) \mathbf{P}^T \left( \frac{\mathbf{x} - \bar{\mathbf{x}}}{\rho} \right) d\Omega_x \right) \mathbf{a}(\bar{\mathbf{x}}) = \int_{\Omega_x} \mathbf{P} \left( \frac{\mathbf{x} - \bar{\mathbf{x}}}{\rho} \right) u(\mathbf{x}) w_\rho(\mathbf{x} - \bar{\mathbf{x}}) d\Omega_x \quad (8)$$

Define the so-called moment matrix  $\mathbf{M}$  as

$$\mathbf{M}(\bar{\mathbf{x}}) = \int_{\Omega_x} \mathbf{P} \left( \frac{\mathbf{x} - \bar{\mathbf{x}}}{\rho} \right) w_\rho(\mathbf{x} - \bar{\mathbf{x}}) \mathbf{P}^T \left( \frac{\mathbf{x} - \bar{\mathbf{x}}}{\rho} \right) d\Omega_x \quad (9)$$

Therefore,  $\mathbf{a}(\bar{\mathbf{x}})$  can be obtained by

$$\mathbf{a}(\bar{\mathbf{x}}) = \mathbf{M}^{-1}(\bar{\mathbf{x}}) \int_{\Omega_x} \mathbf{P} \left( \frac{\mathbf{x} - \bar{\mathbf{x}}}{\rho} \right) u(\mathbf{x}) w_\rho(\mathbf{x} - \bar{\mathbf{x}}) d\Omega_x \quad (10)$$

By substituting the aforementioned  $\mathbf{a}(\bar{\mathbf{x}})$  into Equation (5) and changing the dummy variable  $\mathbf{x}$  in Equation (10) to  $\mathbf{y}$ , it yields

$$u^h(\mathbf{x}) = \mathbf{P}^T \left( \frac{\mathbf{x} - \bar{\mathbf{x}}}{\rho} \right) \mathbf{M}^{-1}(\bar{\mathbf{x}}) \int_{\Omega_y} \mathbf{P} \left( \frac{\mathbf{y} - \bar{\mathbf{x}}}{\rho} \right) u(\mathbf{y}) w_\rho(\mathbf{y} - \bar{\mathbf{x}}) d\Omega_y \quad (11)$$

Moving  $\bar{\mathbf{x}}$  over the whole domain,  $\bar{\mathbf{x}} \rightarrow \mathbf{x}$ , gives

$$u^h(\mathbf{x}) = \mathbf{P}^T(0) \mathbf{M}^{-1}(\mathbf{x}) \int_{\Omega_y} \mathbf{P} \left( \frac{\mathbf{y} - \mathbf{x}}{\rho} \right) u(\mathbf{y}) w_\rho(\mathbf{y} - \mathbf{x}) d\Omega_y \quad (12)$$

$$= \int_{\Omega_y} C_\rho(\mathbf{x}; \mathbf{y} - \mathbf{x}) u(\mathbf{y}) w_\rho(\mathbf{y} - \mathbf{x}) d\Omega_y \quad (13)$$

$$= \int_{\Omega_y} K_\rho(\mathbf{x}; \mathbf{y} - \mathbf{x}) u(\mathbf{y}) d\Omega_y \quad (14)$$

where the correction function  $C_\rho(\mathbf{x}; \mathbf{y} - \mathbf{x})$  is defined as follows:

$$C_\rho(\mathbf{x}; \mathbf{y} - \mathbf{x}) = \mathbf{P}^T(0) \mathbf{M}^{-1}(\mathbf{x}) \mathbf{P} \left( \frac{\mathbf{y} - \mathbf{x}}{\rho} \right) \quad (15)$$

and the moving least-square reproducing kernel function is

$$K_{\varrho}(\mathbf{x}; \mathbf{y} - \mathbf{x}) = C_{\varrho}(\mathbf{x}; \mathbf{y} - \mathbf{x})w_{\varrho}(\mathbf{y} - \mathbf{x}) \quad (16)$$

The discrete counterpart of the aforementioned approximation is

$$u^h(\mathbf{x}) = \mathbf{P}^T(0)\mathbf{M}^{-1}(\mathbf{x}) \sum_{I=1}^{NP} \mathbf{P} \left( \frac{\mathbf{x}_I - \mathbf{x}}{\varrho_I} \right) u_I w_{\varrho}(\mathbf{x}_I - \mathbf{x}) \Delta V_I \quad (17)$$

$$= \sum_{I=1}^{NP} C_{\varrho_I}(\mathbf{x}; \mathbf{x}_I - \mathbf{x}) u_I w_{\varrho}(\mathbf{x}_I - \mathbf{x}) \Delta V_I \quad (18)$$

$$= \sum_{I=1}^{NP} K_{\varrho_I}(\mathbf{x}; \mathbf{x}_I - \mathbf{x}) u_I \Delta V_I \quad (19)$$

$$= \sum_{I=1}^{NP} \Psi_I^{\varrho}(x) u_I \quad (20)$$

where the moment matrix is

$$\mathbf{M}(\mathbf{x}) = \sum_{I=1}^{NP} \mathbf{P} \left( \frac{\mathbf{x}_I - \mathbf{x}}{\varrho_I} \right) w_{\varrho_I}(\mathbf{x}_I - \mathbf{x}) \mathbf{P}^T \left( \frac{\mathbf{x}_I - \mathbf{x}}{\varrho_I} \right) \Delta V_I \quad (21)$$

and the shape function is

$$\Psi_I^{\varrho}(x) = K_{\varrho}(x; x - x_I) \Delta V_I \quad (22)$$

$NP$  is the total number of particles in the support domain.  $\Delta V_I$  is the integration weights associated with the nodes. Note that  $\Psi_I^{\varrho}(x)$  has no Kronecker delta property, that is,  $\Psi_I^{\varrho}(x_J) \neq \delta_{IJ}$ .

The compactly supported window function is constructed using cubic spline function. Assume  $r = \frac{|x - \bar{x}|}{\varrho}$ :

$$w(r) = \begin{cases} \frac{2}{3} - 4r^2 + 4r^3 & \text{for } 0 \leq r \leq \frac{1}{2} \\ \frac{4}{3} - 4r + 4r^2 - 4/3r^3 & \text{for } \frac{1}{2} < r \leq 1 \\ 0 & \text{otherwise} \end{cases} \quad (23)$$

For 2D and rectangular support case, the window function becomes

$$w(\mathbf{x} - \mathbf{x}_I) = w(r_{x1}) \cdot w(r_{x2}) \quad (24)$$

where  $\mathbf{x} = \{x_1, x_2\}$ ,  $\mathbf{x}_I = \{x_{I1}, x_{I2}\}$ ,  $r_{x1} = \frac{|x_1 - x_{I1}|}{\varrho_{I1}}$ ,  $r_{x2} = \frac{|x_2 - x_{I2}|}{\varrho_{I2}}$ . The window function on a rectangular support domain is illustrated in Figure 2.

**3.1.2. Enforcement of essential boundary.** As mentioned in the previous section, the shape function in some meshfree methods (i.e., EGFMRKPM, etc.) does not possess Kronecker delta property, that is,  $\Psi_I^{\varrho}(x_J) \neq \delta_{IJ}$ . Consequently, the essential boundary conditions cannot be directly imposed. Special treatment is therefore required to enforce the essential boundary conditions using, for example, the penalty method (e.g., [3, 6]) or Lagrange multipliers [5]. In this paper, a transformation method proposed by [30] and [31] is used to enforce the essential boundary conditions for the displacement and pore fluid pressure.

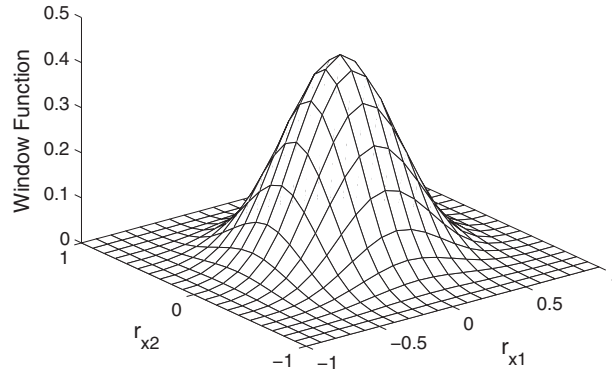


Figure 2. Schematic illustration of a window function on a rectangular support domain.

Let the vector  $\mathbf{d}$  represent a collection of all the nodal field variables ( $\mathbf{u}$  and  $p$ ). The nodes are separated into two groups:  $N_\Gamma$  nodes on the essential boundary and  $N_\Lambda$  nodes in the rest of the domain. The total number of nodes  $NP = N_\Gamma + N_\Lambda$ . Also denote the shape functions associated with the essential boundary nodes by  $\Psi^\Gamma(\mathbf{x})$  and shape functions of the rest nodes by  $\Psi^\Lambda(\mathbf{x})$ . The meshfree approximation of the trial function and test function can be recast as:

$$\mathbf{d}(\mathbf{x}) = \sum_{I=1}^{NP} \Psi_I(\mathbf{x}) d_I = \sum_{I=1}^{N_\Lambda} \Psi_I^\Lambda(\mathbf{x}) d_I^\Lambda + \sum_{I=1}^{N_\Gamma} \Psi_I^\Gamma(\mathbf{x}) d_I^\Gamma = \Psi^\Lambda \mathbf{d}^\Lambda + \Psi^\Gamma \mathbf{d}^\Gamma \quad (25)$$

$$\delta \mathbf{d}(\mathbf{x}) = \sum_{I=1}^{NP} \Psi_I(\mathbf{x}) \delta d_I = \sum_{I=1}^{N_\Lambda} \Psi_I^\Lambda(\mathbf{x}) \delta d_I^\Lambda + \sum_{I=1}^{N_\Gamma} \Psi_I^\Gamma(\mathbf{x}) \delta d_I^\Gamma = \Psi^\Lambda \delta \mathbf{d}^\Lambda + \Psi^\Gamma \delta \mathbf{d}^\Gamma \quad (26)$$

On the essential boundary,  $\mathbf{d}(\mathbf{x}_J) = \bar{\mathbf{d}}(\mathbf{x}_J)$ ,  $\delta \mathbf{d}(\mathbf{x}_J) = 0$ , where  $\bar{\mathbf{d}}(\mathbf{x}_J)$  is the prescribed boundary condition and  $J = 1, 2, \dots, N_\Gamma$ . Therefore,

$$\bar{\mathbf{d}}(\mathbf{x}_J) = \sum_{I=1}^{N_\Lambda} \Psi_I^\Lambda(\mathbf{x}_J) d_I^\Lambda + \sum_{I=1}^{N_\Gamma} \Psi_I^\Gamma(\mathbf{x}_J) d_I^\Gamma \quad (27)$$

$$0 = \sum_{I=1}^{N_\Lambda} \Psi_I^\Lambda(\mathbf{x}_J) \delta d_I^\Lambda + \sum_{I=1}^{N_\Gamma} \Psi_I^\Gamma(\mathbf{x}_J) \delta d_I^\Gamma \quad (28)$$

The aforementioned expression can be written in matrix form as

$$\bar{\mathbf{d}} = \mathbf{D}^\Lambda \mathbf{d}^\Lambda + \mathbf{D}^\Gamma \mathbf{d}^\Gamma \quad (29)$$

$$\mathbf{0} = \mathbf{D}^\Lambda \delta \mathbf{d}^\Lambda + \mathbf{D}^\Gamma \delta \mathbf{d}^\Gamma \quad (30)$$

where  $\bar{\mathbf{d}}_I = \bar{\mathbf{d}}(\mathbf{x}_I)$ ,  $D_{IJ}^\Lambda = \Psi_I^\Lambda(\mathbf{x}_J)$ , and  $D_{IJ}^\Gamma = \Psi_I^\Gamma(\mathbf{x}_J)$ . Therefore,

$$\mathbf{d}^\Gamma = (\mathbf{D}^\Gamma)^{-1} (\bar{\mathbf{d}} - \mathbf{D}^\Lambda \mathbf{d}^\Lambda) \quad (31)$$

$$\delta \mathbf{d}^\Gamma = -(\mathbf{D}^\Gamma)^{-1} \mathbf{D}^\Lambda \delta \mathbf{d}^\Lambda \quad (32)$$

Substituting Equation (31) into the approximation Equation (25) yields

$$\mathbf{d}(\mathbf{x}) = \Psi^\Lambda \mathbf{d}^\Lambda + \Psi^\Gamma (\mathbf{D}^\Gamma)^{-1} (\bar{\mathbf{d}} - \mathbf{D}^\Lambda \mathbf{d}^\Lambda) \quad (33)$$

$$= (\Psi^\Lambda - \Psi^\Gamma (\mathbf{D}^\Gamma)^{-1} \mathbf{D}^\Lambda) \mathbf{d}^\Lambda + \Psi^\Gamma (\mathbf{D}^\Gamma)^{-1} \bar{\mathbf{d}} \quad (34)$$

$$= \mathbf{W}^\Lambda \mathbf{d}^\Lambda + \mathbf{W}^\Gamma \bar{\mathbf{d}} \quad (35)$$

where  $\mathbf{W}^\Lambda = (\Psi^\Lambda - \Psi^\Gamma (\mathbf{D}^\Gamma)^{-1} \mathbf{D}^\Lambda)$  and  $\mathbf{W}^\Gamma = \Psi^\Gamma (\mathbf{D}^\Gamma)^{-1}$  can be interpreted as the transformed shape function. Once  $\mathbf{d}^\Lambda$  is obtained, the approximated  $\mathbf{d}^\Gamma$  on the essential boundary can be further obtained from Equation (31). It has been shown that the essential boundary can be fairly accurately imposed [32].

Similarly, the modified interpolation of test function becomes

$$\delta \mathbf{d}(\mathbf{x}) = \Psi^\Lambda \delta \mathbf{d}^\Lambda + \Psi^\Gamma (\mathbf{D}^\Gamma)^{-1} (-\mathbf{D}^\Lambda \delta \mathbf{d}^\Lambda) \quad (36)$$

$$= (\Psi^\Lambda - \Psi^\Gamma (\mathbf{D}^\Gamma)^{-1} \mathbf{D}^\Lambda) \delta \mathbf{d}^\Lambda \quad (37)$$

$$= \mathbf{W}^\Lambda \delta \mathbf{d}^\Lambda \quad (38)$$

3.1.3. *Semi-discrete form.* The corresponding weak formulations for Equations (2) and (1) are

$$\begin{aligned} & \int_{\Omega} \delta p_{,i} k_{ij} p_{,j} d\Omega + \int_{\Omega} \delta p \dot{u}_{i,i} d\Omega + \int_{\Omega} \delta p \frac{n \dot{p}}{K_f} d\Omega - \int_{\Gamma_p} \delta p q d\Gamma_p \\ & - \int_{\Gamma_w} \delta p \bar{q} d\Gamma_w - \int_{\Omega} \delta p_{,i} k_{ij} \rho_f b_j d\Omega = 0 \end{aligned} \quad (39)$$

$$\begin{aligned} & \int_{\Omega} \delta u_i \rho \ddot{u}_i d\Omega + \int_{\Omega} \delta u_{i,j} \sigma'_{ij} d\Omega - \int_{\Omega} \delta u_{i,j} p \delta_{ij} d\Omega - \int_{\Omega} \delta u_i \rho b_i d\Omega \\ & - \int_{\Gamma_t} \delta u_i \bar{t}_i d\Gamma_t - \int_{\Gamma_u} \delta u_i \sigma'_{ij} n_j d\Gamma_u = 0 \end{aligned} \quad (40)$$

From Section 3.1.2, the approximation for  $p$ ,  $u$ ,  $\delta p$  and  $\delta u$  are given by:

$$p = \sum_{I=1}^{N_\Lambda^p} W_I^{p,\Lambda} p_I^\Lambda + \sum_{I=1}^{N_\Gamma^p} W_I^{p,\Gamma} \bar{p}_I \quad (41)$$

$$u = \sum_{I=1}^{N_\Lambda^u} W_I^{u,\Lambda} u_I^\Lambda + \sum_{I=1}^{N_\Gamma^u} W_I^{u,\Gamma} \bar{u}_I \quad (42)$$

$$\delta p = \sum_{I=1}^{N_\Lambda^p} W_I^{p,\Lambda} \delta p_I^\Lambda \quad (43)$$

$$\delta u = \sum_{I=1}^{N_\Lambda^u} W_I^{u,\Lambda} \delta u_I^\Lambda \quad (44)$$

As argued in [32, Page 119],

$$\int_{\Gamma_p} W_I^{p,\Lambda} \delta p_I^\Lambda \bar{q} d\Gamma_p \approx 0 \quad (45)$$

$$\int_{\Gamma_u} W_I^{u,\Lambda} \delta u_{iI}^\Lambda \sigma'_{ij} n_j d\Gamma_u \approx 0 \quad (46)$$

Plugging the aforementioned discretization of  $p$ ,  $u$ ,  $\delta p$ , and  $\delta u$  into the weak formulations yields the following semi-discrete formulation:

$$\mathbf{Q}^T \dot{\mathbf{u}}^\Lambda + \mathbf{H} \mathbf{p}^\Lambda + \mathbf{S} \dot{\mathbf{p}}^\Lambda - \mathbf{f}^p = \mathbf{0} \quad (47)$$

$$\mathbf{M} \ddot{\mathbf{u}}^\Lambda + \mathbf{K} \mathbf{u}^\Lambda - \mathbf{Q} \mathbf{p}^\Lambda - \mathbf{f}^u = \mathbf{0} \quad (48)$$

where

$$\begin{aligned} \mathbf{H} &= \int_{\Omega} (\nabla \mathbf{W}^{p,\Lambda})^T \mathbf{k} (\nabla \mathbf{W}^{p,\Lambda}) d\Omega \text{ (permeability matrix)} \\ \mathbf{S} &= \int_{\Omega} (\mathbf{W}^{p,\Lambda})^T \frac{n}{K_f} \mathbf{W}^{p,\Lambda} d\Omega \text{ (compressibility matrix)} \\ \mathbf{M} &= \int_{\Omega} (\mathbf{W}^{u,\Lambda})^T \rho \mathbf{W}^{u,\Lambda} d\Omega \text{ (mass matrix)} \\ \mathbf{K} &= \int_{\Omega} (\mathbf{B}^\Lambda)^T \mathbf{C} \mathbf{B}^\Lambda d\Omega \text{ (stiffness matrix)} \\ \mathbf{Q} &= \int_{\Omega} (\mathbf{B}^\Lambda)^T \mathbf{m} \mathbf{W}^{p,\Lambda} d\Omega \text{ (coupling matrix)} \\ \mathbf{f}^p &= \int_{\Gamma_w} (\mathbf{W}^{p,\Lambda})^T \bar{q} d\Gamma_w + \int_{\Omega} (\nabla \mathbf{W}^{p,\Lambda})^T (\mathbf{k} \rho_f \mathbf{b}) d\Omega - \int_{\Omega} (\mathbf{W}^{p,\Lambda})^T \frac{n}{K_f} \mathbf{W}^{p,\Gamma} \dot{\bar{p}} d\Omega \\ &\quad - \int_{\Omega} (\nabla \mathbf{W}^{p,\Lambda})^T \mathbf{k} \nabla \mathbf{W}^{p,\Gamma} \bar{p} d\Omega - \int_{\Omega} (\mathbf{W}^{p,\Lambda})^T \mathbf{m}^T \mathbf{B}^\Gamma \bar{\mathbf{u}} d\Omega \\ \mathbf{f}^u &= \int_{\Gamma_t} (\mathbf{W}^{u,\Lambda})^T \bar{\mathbf{t}} d\Gamma_t + \int_{\Omega} (\mathbf{W}^{u,\Lambda})^T \rho \mathbf{b} d\Omega - \int_{\Omega} \mathbf{W}^{u,\Lambda} \rho \mathbf{W}^{u,\Gamma} \ddot{\bar{\mathbf{u}}} d\Omega \\ &\quad + \int_{\Omega} (\mathbf{B}^\Lambda)^T \mathbf{m} \mathbf{W}^{p,\Gamma} \bar{p} d\Omega - \int_{\Omega} (\mathbf{B}^\Lambda)^T \mathbf{C} \mathbf{B}^\Gamma \bar{\mathbf{u}} d\Omega \end{aligned}$$

and  $\mathbf{m} = [1, 1, 1, 0, 0, 0]^T$ ,  $\mathbf{B}^\Lambda$  and  $\mathbf{B}^\Gamma$  are *strain-displacement* matrix corresponding to  $\mathbf{W}^\Lambda$  and  $\mathbf{W}^\Gamma$  respectively and are given by

$$\mathbf{B}_I^\Lambda = \begin{Bmatrix} W_{I,x}^\Lambda & 0 \\ 0 & W_{I,y}^\Lambda \\ W_{I,y}^\Lambda & W_{I,x}^\Lambda \end{Bmatrix}, \quad \mathbf{B}_I^\Gamma = \begin{Bmatrix} W_{I,x}^\Gamma & 0 \\ 0 & W_{I,y}^\Gamma \\ W_{I,y}^\Gamma & W_{I,x}^\Gamma \end{Bmatrix} \quad (49)$$

It is worth pointing out that the vectors  $\mathbf{f}^p$  and  $\mathbf{f}^u$  are contributed not only from the boundary integration of prescribed variables and the domain integration of body force (same as the conventional FEM formulation) but also additional terms (underlined) consisting of the domain integrations of the prescribed boundary values. This is due to the lack of Kronecker delta properties of the RKPM shape functions. In the aforementioned expression,  $\mathbf{K}\mathbf{u}^\Lambda$  can also be represented as  $\int_{\Omega} (\mathbf{B}^\Lambda)^T \boldsymbol{\sigma}' d\Omega$ , in which case the effective stress  $\boldsymbol{\sigma}'$  is updated incrementally through constitutive relationship  $\dot{\boldsymbol{\sigma}}' = \mathbf{C} : \dot{\boldsymbol{\varepsilon}}$ . In the following sections,  $\mathbf{p}^\Lambda$  and  $\mathbf{u}^\Lambda$  will be simply represented as  $\mathbf{p}$  and  $\mathbf{u}$  for convenience.

### 3.2. Temporal discretization

In this paper, different methods are used for temporal discretization of fluid and solid solvers. For the fluid solver, Equation (47), the generalized trapezoidal rule is adopted as follows:

$$\dot{\mathbf{p}}_{n+\theta} = (\mathbf{p}_{n+1} - \mathbf{p}_n) / \Delta t_f \quad (50)$$

$$\mathbf{p}_{n+\theta} = (1 - \theta)\mathbf{p}_n + \theta\mathbf{p}_{n+1} \quad (51)$$

$$\dot{\mathbf{u}}_{n+\theta} = (\mathbf{u}_{n+1} - \mathbf{u}_n) / \Delta t_f \quad (52)$$

$$\mathbf{u}_{n+\theta} = (1 - \theta)\mathbf{u}_n + \theta\mathbf{u}_{n+1} \quad (53)$$

where  $\Delta t_f = t_{n+1} - t_n$ , corresponding to real time increment.  $\theta$  may vary between 0 and 1 and  $0.5 \leq \theta \leq 1$  is required for unconditional stability. In this paper,  $\theta = 1$  is used.

An explicit predictor-corrector scheme as described in [33] is employed to solve Equation (48). Details will be elaborated in the next section and Table I.

## 4. ITERATIVE COUPLING SCHEME

As mentioned in the introduction, this paper adopts an iterative way to solve the coupled system of equations. The fluid solver is executed first to update the fluid pressure  $p$ , which is then substituted into the solid solver to update the solid displacement  $\mathbf{u}$ . Iterations between these two solvers are needed to obtain a compatible pair of  $\mathbf{u}$  and  $p$  solutions. The iterative scheme, however, would be numerically unstable. Therefore, an additional term, called the stabilization term in this paper, is introduced to the fluid continuity equation to regulate the system. The stabilization term employs the variation of pore fluid pressure between two successive iterations. The governing equations is recast for the time step  $t_n, t_{n+1}$  and iteration number  $i, i + 1$  as follows.

Fluid solver:

$$(\mathbf{H}\Delta t_f + \mathbf{S})\mathbf{p}_{n+1}^{(i+1)} + \boxed{\tilde{\mathbf{S}}(\mathbf{p}_{n+1}^{(i+1)} - \mathbf{p}_{n+1}^{(i)})} + \mathbf{Q}^T(\mathbf{u}_{n+1}^{(i)} - \mathbf{u}_n) - \mathbf{S}\mathbf{p}_n - \mathbf{f}_{n+1}^p \Delta t_f = 0 \quad (54)$$

Solid solver:

$$\mathbf{M}\ddot{\mathbf{u}}_{n+1}^{(i+1,k+1)} + \tilde{\mathbf{C}}_{n+1}^{(i+1,k)}\dot{\mathbf{u}}_{n+1}^{(i+1,k)} + \mathbf{K}_{n+1}^{(i+1,k)}\mathbf{u}_{n+1}^{(i+1,k)} - \mathbf{Q}\mathbf{p}_{n+1}^{(i+1)} - \mathbf{f}_{n+1}^u = 0 \quad (55)$$

In the aforementioned equations, subscripts  $n$  and  $n + 1$  denote the variables at the real time step  $t_n$  and  $t_{n+1}$ , respectively.  $\mathbf{p}_n$  and  $\mathbf{u}_n$  are known solutions of pressure and displacement at  $t_n$ . During the iterations within one time step, the fluid solver and solid solver are executed sequentially and iteratively, with iteration numbers denoted by superscripts  $i, i + 1 \dots$  (e.g.,  $\mathbf{p}_{n+1}^{(i)}, \mathbf{p}_{n+1}^{(i+1)}, \mathbf{u}_{n+1}^{(i+1,*)}$ ). The fluid solver solves the pressure at once implicitly, while the solid solver solves the displacement explicitly through iterations, denoted by superscripts  $k, k + 1 \dots$  (e.g.,  $\mathbf{u}_{n+1}^{(i+1,k)}, \mathbf{u}_{n+1}^{(i+1,k+1)}$ ). It is also noted that a damping matrix  $\tilde{\mathbf{C}}$  is included in the solid solver. As stated before, the fluid solver

Table I. Iterative algorithm.

<p>1. Initialization at the start of time: <math>\mathbf{p}_0 = \mathbf{p}_{ini}</math>, <math>\mathbf{u}_0 = \mathbf{u}_{ini}</math>.</p> <p>2. Start time integration. <math>n</math> starts from 0.</p> <p>(a) Initialization <math>\mathbf{p}_{n+1}^{(0)} = \mathbf{p}_n</math>, <math>\mathbf{u}_{n+1}^{(0)} = \mathbf{u}_n</math>, update <math>\mathbf{f}_{n+1}^u</math> and <math>\mathbf{f}_{n+1}^p</math>.</p> <p>(b) Start iteration scheme. <math>i</math> starts at 0.</p> <p>i. Call fluid solver to solve for <math>\mathbf{p}_{n+1}^{(i+1)}</math>:</p> $\mathbf{p}_{n+1}^{(i+1)} = (\mathbf{H}\Delta t_f + \mathbf{S} + \tilde{\mathbf{S}})^{-1} [\tilde{\mathbf{S}}\mathbf{p}_{n+1}^{(i)} - \mathbf{Q}^T (\mathbf{u}_{n+1}^{(i)} - \mathbf{u}_n) + \mathbf{S}\mathbf{p}_n + \mathbf{f}_{n+1}^p \Delta t_f].$ <p>ii. Call solid solver adopting predictor-corrector integration method. <math>k</math> starts from 0.</p> <p>A. Compute the predictors:</p> $\tilde{\mathbf{u}}_{n+1}^{(i+1,k+1)} = \mathbf{u}_{n+1}^{(i+1,k)} + \Delta t \mathbf{v}_{n+1}^{(i+1,k)} + \frac{(\Delta t)^2}{2} (1 - 2\beta) \ddot{\mathbf{u}}_{n+1}^{(i+1,k)}$ $\tilde{\mathbf{v}}_{n+1}^{(i+1,k+1)} = \mathbf{v}_{n+1}^{(i+1,k)} + (1 - \gamma) \Delta t \ddot{\mathbf{u}}_{n+1}^{(i+1,k)}$ <p>A pseudo-time step <math>\Delta t = 10^{-5}s</math> is used for quasi-static problems.</p> <p>B. Update <math>\tilde{\mathbf{K}}_{n+1}^{(i+1,k+1)} = \int_{\Omega} \mathbf{B}^T \mathbf{C} (\nabla^s \tilde{\mathbf{u}}_{n+1}^{(i+1,k+1)}) \mathbf{B} d\Omega</math> for nonlinear materials.</p> <p>C. Compute</p> $\ddot{\mathbf{u}}_{n+1}^{(i+1,k+1)} = \mathbf{M}^{-1} (\mathbf{Q}\mathbf{p}_{n+1}^{(i+1)} + \mathbf{f}_{n+1}^u - \tilde{\mathbf{C}}\tilde{\mathbf{v}}_{n+1}^{(i+1,k+1)} - \tilde{\mathbf{K}}_{n+1}^{(i+1,k+1)}\tilde{\mathbf{u}}_{n+1}^{(i+1,k+1)})$ <p>D. Compute the correctors:</p> $\mathbf{u}_{n+1}^{(i+1,k+1)} = \tilde{\mathbf{u}}_{n+1}^{(i+1,k+1)} + \beta(\Delta t)^2 \ddot{\mathbf{u}}_{n+1}^{(i+1,k+1)}$ $\mathbf{v}_{n+1}^{(i+1,k+1)} = \tilde{\mathbf{v}}_{n+1}^{(i+1,k+1)} + \gamma \Delta t \ddot{\mathbf{u}}_{n+1}^{(i+1,k+1)}$ <p>E. Check whether <math>\frac{\ \mathbf{F}_{unbal}\ }{\ \mathbf{F}_{tot}\ } \leq TOL_{unbal}</math>.</p> <p>If <i>NO</i>, <math>k \leftarrow k + 1</math> and go to 2(b)iiA.</p> <p>F. End solid solver. Commit <math>\mathbf{u}_{n+1}^{(i+1)} = \mathbf{u}_{n+1}^{(i+1,k+1)}</math>.</p> <p>iii. Check whether both the solutions <math>\mathbf{p}_{n+1}^{(i+1)}</math> and <math>\mathbf{u}_{n+1}^{(i+1)}</math> satisfy the convergence criteria, i.e., <math>\frac{\ \mathbf{p}_{n+1}^{(i+1)} - \mathbf{p}_{n+1}^{(i)}\ }{\ \mathbf{p}_{n+1}^{(i)}\ } \leq TOL_p</math> and <math>\frac{\ \mathbf{u}_{n+1}^{(i+1)} - \mathbf{u}_{n+1}^{(i)}\ }{\ \mathbf{u}_{n+1}^{(i)}\ } \leq TOL_u</math>. If <i>NO</i>, <math>i \leftarrow i + 1</math>, and go to 2(b)i.</p> <p>iv. End iteration scheme.</p> <p>(c) Update <math>\mathbf{p}</math> and <math>\mathbf{u}</math>: <math>\mathbf{p}_{n+1} = \mathbf{p}_{n+1}^{(i+1)}</math> and <math>\mathbf{u}_{n+1} = \mathbf{u}_{n+1}^{(i+1)}</math>.</p> <p>(d) If <math>n &lt;</math> total time steps, <math>n \leftarrow n + 1</math>, and go to 2(a).</p> <p>3. End of time integration.</p>
--

and solid solver are executed sequentially and iteratively. Nested numerical iterations (denoted by subscript  $n$  and superscripts  $i, k$ ) are therefore required to solve the system. The procedure for time marching from  $t_n$  to  $t_{n+1}$  is summarized in Table I.

The boxed term in Equation (54) is the stabilization term introduced to stabilize the system.  $\tilde{\mathbf{S}}$  is formulated as  $\int_{\Omega} (\mathbf{W}^{p,\Lambda})^T \frac{1}{K_r} \mathbf{W}^{p,\Lambda} d\Omega$  to have a similar form as the compressibility matrix  $\mathbf{S}$ , where  $K_r$  is an introduced relaxation parameter. The choice of  $K_r$  parameter will affect the numerical stability and convergence rate of the algorithm, and it will be determined in the next section. The stabilization term is also related to the variation of pressure increment between successive iterations. It vanishes when a converged pressure solution  $\mathbf{p}_{n+1}^{(i+1)} \rightarrow \mathbf{p}_{n+1}^{(i)}$  is achieved. In this case, the algorithm results in a consistent pair of displacement and pore water pressure

solution. It should be noted that the bulk modulus of the fluid is much greater than that of the solid skeleton in most practical cases concerned. Without the stabilization term, iterations between two systems with vastly different stiffness would be unstable and divergent. At best, a very stringent time step should be used. The stability of the algorithm will be proved by stability analysis in Section 5.

In Table I,  $\mathbf{v} = \dot{\mathbf{u}}$  is the velocity vector,  $\mathbf{F}_{unbal}$  the unbalanced force and  $\mathbf{F}_{tot}$  the total applied force.  $TOL_{unbal}$ ,  $TOL_p$  and  $TOL_u$  are tolerances for the unbalanced force, pore water pressure variation and solid displacement variation, respectively.  $\mathbf{C}(\nabla^s \tilde{\mathbf{u}}_{n+1}^{(i+1,k+1)})$  denotes stiffness matrix as a function of displacement.  $\beta$  and  $\gamma$  are the two parameters for numerical integration. In the simulations presented in this paper,  $\beta = 0.25$  and  $\gamma = 0.5$  are used.  $\tilde{\mathbf{C}}$  is taken as the conventional Rayleigh damping matrix given by  $\tilde{\mathbf{C}} = a_R \mathbf{M} + b_R \mathbf{K}$ , where  $a_R$  and  $b_R$  can be estimated from the specific problem studied.

It should also be pointed out that for the simplicity of presentations, some variables in Table I are expressed using inversed global matrices. The matrix inversion may be undesirable if a large scale problem is considered. In actual numerical implementation, however, these inverse matrix can be solved by alternative numerical methods. For example, the mass matrix in Table I step 2(b)iiC can be approximated as a diagonally-lumped mass matrix, and inversion of the mass matrix can be readily obtained.

Different time integration strategies are employed in the proposed scheme. The fluid solver is formulated using implicit time integration for pressure, while displacement is solved explicitly. This is because the fluid solver is generally more 'linear' and can be effectively solved implicitly, while highly nonlinear constitutive model for the solid skeleton may be used, making an implicit method much more difficult to be implemented in the solid solver.

The solid solver demonstrated in Table I is used to solve quasi-static problems.  $\Delta t$  serves as a virtual time step and is much smaller than  $\Delta t_f$ . The quasi-static problem is solved through the numerically-damped dynamic system when the unbalanced force is sufficiently small (via step 2(b)iiE). However, the scheme can also be applied to solve dynamic problems.  $\Delta t$  is then the real time increment for the solid solver, and it can be chosen to be equal to or less than the fluid time step  $\Delta t_f$ . In this case, the solid solver is executed for one or several steps ( $n_s \geq 1$ ), then followed by one step in the fluid solver such that  $n_s \Delta t = \Delta t_f$ . Conversely, the code can be readily modified to consider the case that one solid time step corresponds to one or several fluid time step(s). Note also that the damping matrix should take real damping instead of numerical damping in solving dynamic problems.

## 5. STABILITY ANALYSIS

Based on the iterative scheme described in Section 4, numerical stability needs to be examined at three levels, that is, stability of individual solvers, stability during the one iteration step (i.e.,  $i \rightarrow i + 1$ , called *iteration stability* hereafter) and stability during time marching (i.e.,  $n \rightarrow n + 1$ , called *staggered stability* hereafter). It should be noted that the stability at the former level is a prerequisite for the stability at the latter level. A stable iterative coupling scheme requires stability at all three levels. In this work, the *iteration stability* analysis is analyzed in two ways, namely, perturbation theory [34] and error propagation method [35]. For simplicity, it is assumed that the solid skeleton is linearly elastic.

### 5.1. Stability of individual solvers

As shown in Section 4, the equation of momentum equilibrium can be solved in an explicit way. The stability criterion for the solid solver can be therefore estimated by ensuring that the calculation front is always ahead of the propagating wave front, that is,  $\Delta t < L/v_w$ , where  $L$  is the distance between nodes, and  $v_w$  is the wave speed. On the other hand, the fluid solver is unconditionally stable using a fully implicit integration scheme.

## 5.2. Iteration stability

The *iteration stability* is analyzed using both perturbation theory and error propagation method. The formulations with and without the stabilization term are analyzed to demonstrate the effectiveness of the stabilization technique.

**5.2.1. Perturbation theory.** Assume a stable pair of ( $\mathbf{p}$  and  $\mathbf{u}$ ) solutions is given during each iteration ( $i$ ) by the two solvers. The equations for the fluid solver at two successive iterations  $i$  and  $i + 1$  are given by

$$(\mathbf{H}\Delta t_f + \mathbf{S})\mathbf{p}_{n+1}^{(i+1)} + \tilde{\mathbf{S}}(\mathbf{p}_{n+1}^{(i+1)} - \mathbf{p}_{n+1}^{(i)}) + \mathbf{Q}^T(\mathbf{u}_{n+1}^{(i)} - \mathbf{u}_n) - \mathbf{S}\mathbf{p}_n - \mathbf{f}_{n+1}^p \Delta t_f = 0 \quad (56)$$

$$(\mathbf{H}\Delta t_f + \mathbf{S})\mathbf{p}_{n+1}^{(i)} + \tilde{\mathbf{S}}(\mathbf{p}_{n+1}^{(i)} - \mathbf{p}_{n+1}^{(i-1)}) + \mathbf{Q}^T(\mathbf{u}_{n+1}^{(i-1)} - \mathbf{u}_n) - \mathbf{S}\mathbf{p}_n - \mathbf{f}_{n+1}^p \Delta t_f = 0 \quad (57)$$

Subtracting Equation (57) from (56) yields

$$(\mathbf{H}\Delta t_f + \mathbf{S} + \tilde{\mathbf{S}})(\mathbf{p}_{n+1}^{(i+1)} - \mathbf{p}_{n+1}^{(i)}) - \tilde{\mathbf{S}}(\mathbf{p}_{n+1}^{(i)} - \mathbf{p}_{n+1}^{(i-1)}) + \mathbf{Q}^T(\mathbf{u}_{n+1}^{(i)} - \mathbf{u}_{n+1}^{(i-1)}) = 0 \quad (58)$$

Likewise, the following equation holds for the solid solver for  $\mathbf{p}$  and  $\mathbf{u}$  at iteration  $i - 1$  and  $i$ :

$$-\mathbf{Q}(\mathbf{p}_{n+1}^{(i)} - \mathbf{p}_{n+1}^{(i-1)}) + \mathbf{K}(\mathbf{u}_{n+1}^{(i)} - \mathbf{u}_{n+1}^{(i-1)}) = 0 \quad (59)$$

Assuming  $\mathbf{K}$  is invertible, the aforementioned equation can be further written as

$$(\mathbf{u}_{n+1}^{(i)} - \mathbf{u}_{n+1}^{(i-1)}) = \mathbf{K}^{-1}\mathbf{Q}(\mathbf{p}_{n+1}^{(i)} - \mathbf{p}_{n+1}^{(i-1)}) \quad (60)$$

Substituting Equation (60) into (58), the variations of pore fluid pressure during three successive iterations can be related by

$$(\mathbf{p}_{n+1}^{(i+1)} - \mathbf{p}_{n+1}^{(i)}) = \underbrace{(\mathbf{H}\Delta t_f + \mathbf{S} + \tilde{\mathbf{S}})^{-1}(-\mathbf{Q}^T\mathbf{K}^{-1}\mathbf{Q} + \tilde{\mathbf{S}})}_{\mathbf{A}}(\mathbf{p}_{n+1}^{(i)} - \mathbf{p}_{n+1}^{(i-1)}) \quad (61)$$

A stable and convergent solution of  $\mathbf{p}$  during the iterations necessitates that the variation between the two successive iterations should decrease as the iteration continues. That is to say, the left side of Equation (61) should approach zero and finally vanish as  $i$  increases. To achieve this, it is required that,  $\|\mathbf{A}\|$ , the spectral norm of the amplification matrix  $\mathbf{A}$ , must satisfy

$$\|\mathbf{A}\| < 1. \quad (62)$$

With a properly selected stabilization term  $\tilde{\mathbf{S}}$ , Equation (62) can be satisfied unconditionally with no limit imposed on the time step size  $\Delta t_f$ . As is self-evident, the stabilization term would influence the amplification matrix, and therefore influence the convergence rate of the iterations. The closer  $\|\mathbf{A}\|$  approaches zero, the faster the solution would converge. Different convergence performances with different choices of  $K_r$  will be demonstrated in the numerical simulations in Section 6.

The iterative scheme is reduced to being conditionally stable if without the stabilization term, the stability criterion imposed on the amplification matrix becomes

$$\|(\mathbf{H}\Delta t_f + \mathbf{S})^{-1}(-\mathbf{Q}^T\mathbf{K}^{-1}\mathbf{Q})\| < 1. \quad (63)$$

For a boundary value problem, coefficient matrices  $\mathbf{H}$ ,  $\mathbf{S}$  and  $\mathbf{K}$  usually remain unchanged. Therefore, the range of time step  $\Delta t_f$  for a stable iterative scheme is constrained by Equation (63). A large  $\Delta t_f$  is thus required for general geotechnical practice.

5.2.2. *Error propagation method.* Denote by  $(\tilde{\mathbf{p}}, \tilde{\mathbf{u}})$  the ‘true’ solutions.  $\mathbf{r}_{n+1}^p$  and  $\mathbf{r}_{n+1}^u$  are the local truncation errors due to temporal discretization. Equation (64) is the fluid equation with the ‘true’ solutions and truncation errors implemented:

$$(\mathbf{H}\Delta t_f + \mathbf{S}) \tilde{\mathbf{p}}_{n+1} + \tilde{\mathbf{S}}(\tilde{\mathbf{p}}_{n+1} - \tilde{\mathbf{p}}_n) + \mathbf{Q}^T(\tilde{\mathbf{u}}_{n+1} - \tilde{\mathbf{u}}_n) - \mathbf{S}\tilde{\mathbf{p}}_n - \mathbf{f}_{n+1}^p \Delta t_f = \mathbf{r}_{n+1}^p \quad (64)$$

By subtracting Equation (56) from (64) and denoting the error between the ‘true’ solution and the numerical solution by  $\mathbf{e}_n^{p,(i)} = \tilde{\mathbf{p}}_n - \mathbf{p}_n^{(i)}$ , it yields

$$(\mathbf{H}\Delta t_f + \mathbf{S} + \tilde{\mathbf{S}}) \mathbf{e}_{n+1}^{p,(i+1)} - \tilde{\mathbf{S}}\mathbf{e}_{n+1}^{p,(i)} + \mathbf{Q}^T(\mathbf{e}_{n+1}^{u,(i)} - \mathbf{e}_n^u) - \mathbf{S}\mathbf{e}_n^p = \mathbf{r}_{n+1}^p \quad (65)$$

Similarly, the error for the displacement is denoted by  $\mathbf{e}_n^{u,(i)} = \tilde{\mathbf{u}}_n - \mathbf{u}_n^i$ . Error terms in the solid solver can be obtained by performing similar algebraic manipulations:

$$-\mathbf{Q}\mathbf{e}_{n+1}^{p,(i)} + \mathbf{K}\mathbf{e}_{n+1}^{u,(i)} = \mathbf{r}_{n+1}^u \quad (66)$$

$$-\mathbf{Q}\mathbf{e}_n^p + \mathbf{K}\mathbf{e}_n^u = \mathbf{r}_n^u \quad (67)$$

Subtracting Equation (67) from (66) gives

$$\mathbf{e}_{n+1}^{u,(i)} - \mathbf{e}_n^u = \mathbf{K}^{-1}\mathbf{Q}(\mathbf{e}_{n+1}^{p,(i)} - \mathbf{e}_n^p) + \mathbf{K}^{-1}(\mathbf{r}_{n+1}^u - \mathbf{r}_n^u) \quad (68)$$

Substituting Equation (68) into (65) yields the following derivations:

$$\begin{aligned} & (\mathbf{H}\Delta t_f + \mathbf{S} + \tilde{\mathbf{S}}) \mathbf{e}_{n+1}^{p,(i+1)} - \tilde{\mathbf{S}}\mathbf{e}_{n+1}^{p,(i)} + \mathbf{Q}^T\mathbf{K}^{-1}\mathbf{Q}(\mathbf{e}_{n+1}^{p,(i)} - \mathbf{e}_n^p) \\ & + \mathbf{Q}^T\mathbf{K}^{-1}(\mathbf{r}_{n+1}^u - \mathbf{r}_n^u) - \mathbf{S}\mathbf{e}_n^p = \mathbf{r}_{n+1}^p \\ \Rightarrow & \underbrace{(\mathbf{H}\Delta t_f + \mathbf{S} + \tilde{\mathbf{S}})}_{\mathbf{A}'} \mathbf{e}_{n+1}^{p,(i+1)} = \underbrace{(\tilde{\mathbf{S}} - \mathbf{Q}^T\mathbf{K}^{-1}\mathbf{Q})}_{\mathbf{B}'} \mathbf{e}_{n+1}^{p,(i)} + \underbrace{(\mathbf{S} + \mathbf{Q}\mathbf{K}^{-1}\mathbf{Q})}_{\mathbf{C}'} \mathbf{e}_n^p \\ & + \underbrace{\mathbf{r}_{n+1}^p - \mathbf{Q}^T\mathbf{K}^{-1}(\mathbf{r}_{n+1}^u - \mathbf{r}_n^u)}_{\mathbf{r}'_{n+1}} \quad (69) \\ \Rightarrow & \mathbf{e}_{n+1}^{p,(i+1)} = \underbrace{(\mathbf{A}')^{-1}\mathbf{B}'}_{\mathbf{G}} \mathbf{e}_{n+1}^{p,(i)} + \underbrace{(\mathbf{A}')^{-1}\mathbf{C}'}_{\mathbf{H}'} \mathbf{e}_n^p + (\mathbf{A}')^{-1}\mathbf{r}'_{n+1} \\ \Rightarrow & \mathbf{e}_{n+1}^{p,(i+1)} = \mathbf{G}\mathbf{e}_{n+1}^{p,(i)} + \mathbf{H}'\mathbf{e}_n^p + (\mathbf{A}')^{-1}\mathbf{r}'_{n+1} \\ \Rightarrow & \mathbf{e}_{n+1}^{p,(i+1)} = \mathbf{G}^{i+1}\mathbf{e}_{n+1}^{p,(0)} + \sum_{l=0}^i \mathbf{G}^l\mathbf{H}'\mathbf{e}_n^p + \sum_{l=0}^i \mathbf{G}^l(\mathbf{A}')^{-1}\mathbf{r}'_{n+1} \\ \Rightarrow & \mathbf{e}_{n+1}^{p,(i+1)} = \mathbf{G}^{i+1}\mathbf{e}_{n+1}^{p,(0)} + (\mathbf{I} - \mathbf{G}^{i+1})(\mathbf{I} - \mathbf{G})^{-1}\mathbf{H}'\mathbf{e}_n^p + (\mathbf{I} - \mathbf{G}^{i+1})(\mathbf{I} - \mathbf{G})^{-1}(\mathbf{A}')^{-1}\mathbf{r}'_{n+1} \end{aligned}$$

Therefore, to ensure the error does not grow during the iterations (with increasing  $i$ ), the spectral norm of  $\mathbf{G}$  should be

$$\|\mathbf{G}\| = \|(\mathbf{A}')^{-1}\mathbf{B}'\| = \left\| \left( \mathbf{H}\Delta t_f + \mathbf{S} + \tilde{\mathbf{S}} \right)^{-1} \left( \tilde{\mathbf{S}} - \mathbf{Q}^T\mathbf{K}^{-1}\mathbf{Q} \right) \right\| < 1 \quad (70)$$

This stability criterion is identical to that of Equation (62).

### 5.3. Staggered stability

This part is to prove that the error does not grow during the time marching (i.e.,  $t_0 \rightarrow t_1 \rightarrow \dots \rightarrow t_n$ ). The error in Equation (69) can be further written as

$$\begin{aligned} \mathbf{e}_{n+1}^{p,(i+1)} &= \underbrace{\mathbf{G}^{i+1}}_{\mathbf{L}_{n+1}} \mathbf{e}_{n+1}^{p,(0)} + \underbrace{(\mathbf{I} - \mathbf{G}^{i+1})(\mathbf{I} - \mathbf{G})^{-1} \mathbf{H}'}_{\mathbf{M}_{n+1}} \mathbf{e}_n^p + \underbrace{(\mathbf{I} - \mathbf{G}^{i+1})(\mathbf{I} - \mathbf{G})^{-1} (\mathbf{A}')^{-1}}_{\mathbf{N}_{n+1}} \mathbf{r}'_{n+1} \\ \Rightarrow \mathbf{e}_{n+1}^{p,(i+1)} &= \mathbf{L}_{n+1} \mathbf{e}_{n+1}^{p,(0)} + \mathbf{M}_{n+1} \mathbf{e}_n^p + \mathbf{N}_{n+1} \mathbf{r}'_{n+1} \\ \Rightarrow \mathbf{e}_{n+1}^{p,(i+1)} &= \mathbf{L}_{n+1} \mathbf{e}_{n+1}^{p,(0)} + \sum_{l=0}^n \mathbf{M}_{n+1} \cdots \mathbf{M}_{n+1-l} \mathbf{L}_{n-l} \mathbf{e}_{n-l}^{p,(0)} \\ &\quad + \mathbf{M}_{n+1} \cdots \mathbf{M}_0 \mathbf{e}_0^p + \sum_{l=0}^n \mathbf{M}_{n+1} \cdots \mathbf{M}_{n+1-l} \mathbf{N}_{n-l} \mathbf{r}'_{n-l} + \mathbf{N}_{n+1} \mathbf{r}'_{n+1} \end{aligned} \quad (71)$$

If a full iteration (i.e.,  $i$  is large enough) is adopted, then  $\mathbf{L} = \mathbf{G}^i \rightarrow 0$ ; In the case when  $\mathbf{G} = 0$ ,  $\mathbf{L} = 0$ , the first two terms on the right side in the Equation (71) vanish. Also considering that the truncation error  $\mathbf{r}' \propto O(\Delta t^2)$ , the following criterion is required to ensure the stability of the staggered procedure:

$$\|\mathbf{M}\| = \|(\mathbf{I} - \mathbf{G}^{i+1})(\mathbf{I} - \mathbf{G})^{-1} \mathbf{H}'\| < \|(\mathbf{H} \Delta t_f + \mathbf{S} + \mathbf{Q}^T \mathbf{K}^{-1} \mathbf{Q})^{-1} (\mathbf{S} + \mathbf{Q}^T \mathbf{K}^{-1} \mathbf{Q})\| < 1. \quad (72)$$

The aforementioned inequality can be automatically satisfied if Equation (70) is guaranteed, that is, the staggered procedure is unconditionally stable.

## 6. NUMERICAL EXAMPLES

In this section, three numerical examples are conducted to verify the proposed iterative coupling scheme. The first two examples are consolidation of one-dimensional and two-dimensional soil ground under surcharge. In these examples, the soil is assumed to be linearly elastic, isotropic and homogeneous. The permeability and porosity are assumed to remain constant. The numerical results from these examples are compared with the analytical solutions. The 1D consolidation example also serves as a benchmark problem for studying the influence of relaxation parameter and RKPM support size on the convergence rate of the algorithm.

A fully nonlinear soil model is implemented in the third example. The porosity of the solid phase also varies during the loading process. Permeability is assumed constant, though. In all the numerical examples,  $\mathbf{u}$  and  $p$  share the same RKPM nodal distribution and have the same support size unless otherwise specified.

### 6.1. One-dimensional consolidation of elastic ground

**6.1.1. Model description.** The model set-up for 1D consolidation is illustrated in Figure 3. The height of the soil ground  $h = 10$  m and the domain is spatially discretized using  $5 \times 21$  evenly-distributed RKPM nodes. The material is linearly elastic with Young's modulus  $E = 10$  MPa and Poisson's ratio  $\nu = 0.2$ . The porosity is  $n = 0.3$ . The bulk modulus of fluid is  $K_f = 2.2$  GPa. The isotropic hydraulic conductivity  $k_H = 5 \times 10^{-8}$  m/s. The base and the side boundaries are impermeable and the ground surface is a free-drainage boundary. The base nodes are fixed in the vertical displacement and free to move in the horizontal direction; the side boundaries are fixed in the horizontal direction and free to move in the vertical direction. A constant load of 20 kPa is instantly applied on the top surface at the beginning of the simulation and remains constant during the consolidation process. No body force (e.g., gravitational force) is considered. It is assumed that the initial pore pressure  $p_0 = 20$  kPa and the effective stress is zero in the soil ground, respectively. In this example, the RKPM support size is chosen as 1.5 times of particle intervals and the relaxation parameter  $K_r$  equals the constrained modulus of the soil (i.e.,  $K_r = M_c \equiv K + 4/3G$ ). The numerical tolerances during iterations are set as  $TOL_p = TOL_u = 10^{-3}$ . The time marching

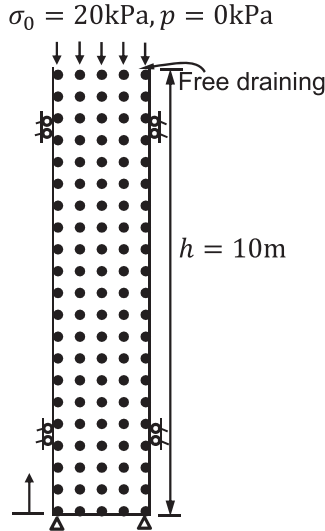


Figure 3. 1D consolidation model setup.

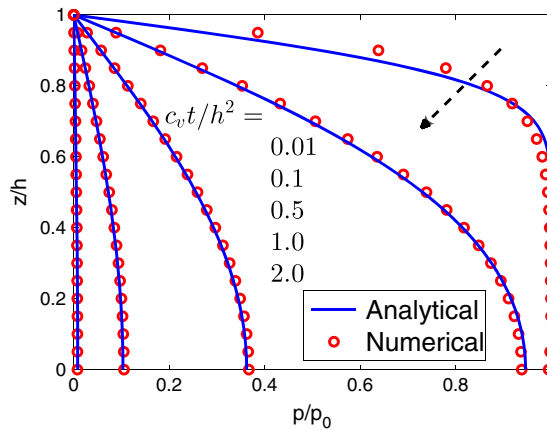


Figure 4. Normalized isochrones distribution of  $p$ .

increment  $\Delta t_f = 5$  h, which can be normalized into a dimensionless measure,  $c_v \Delta t_f / h^2 = 0.01$ , where  $c_v$  is the so-called *coefficient of consolidation* given by  $c_v = k / (M_c + n / K_f)$ .

The pore water pressure distributions along the mid-column particles at the nondimensional time measure  $c_v t / h^2 = 0.01, 0.1, 0.5, 1, 2$  are compared with the analytical solutions, as shown in Figure 4, where the dashed arrow shows the direction of time marching. The degree of consolidation  $U$  is defined as  $U = \frac{u_t - u_0}{u_\infty - u_0}$ , where  $u_t, u_0, u_\infty$  are surface displacement at time  $t$ , initial time and infinite time, respectively [36, Chapter 16]. Figure 5 compares  $U$  obtained from numerical simulation and analytical solution [36, Chapter 16]. The close agreement between the analytical solutions and numerical results indicates that the iterative coupling algorithm can effectively solve the coupled soil-fluid system.

Figure 6 plots the relative error norms of the pore fluid pressure and soil displacement during the first few iteration steps. In general, the relative error norm convergences to zero logarithmically so only 2 or 3 iterations are needed to reduce it to  $10^{-3}$ . Figure 7 also shows the number of iterations required for every time marching step during the simulation at time  $c_v t / h^2 \leq 1$ . In most cases, only 2 iterations are needed to meet the required error tolerance. As the pore pressure continues dissipating, the tolerance criterion becomes tighter and tighter, spikes in the iteration numbers would

consequently appear. Since at time  $c_v t/h^2 = 1$ , most of the pore pressure has been dissipated, the iterative scheme is overall very efficient.

**6.1.2. Influence of relaxation parameter.** The iteration count in this study is a direct measure of convergence rate, which is mainly controlled by the relaxation parameter  $K_r$ . In practice, it is critical to search for a reasonable relaxation parameter, if not the optimal one, to reduce the number of iterations and the computational cost. Using the benchmark problem, simulations with different relaxation parameters ( $K_r = 0.5Mc, 0.75Mc, 1.25Mc, 1.5Mc$ ) are conducted to investigate its effect on the convergence behaviors. Comparisons of the iteration numbers with different relaxation parameters are shown in Figure 8. The results show that there is an optimal relaxation parameter,

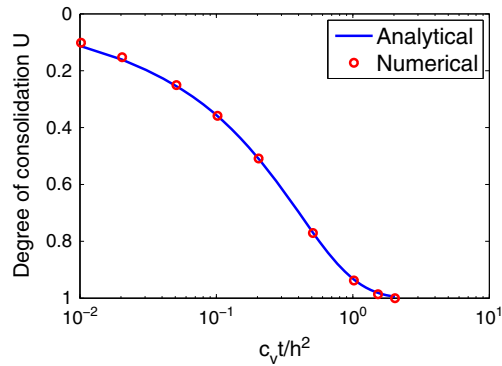


Figure 5. Comparison of surface settlement.

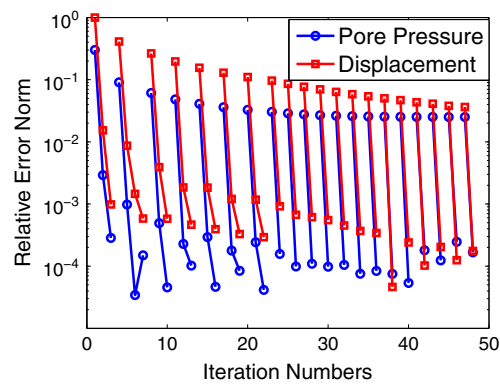


Figure 6. Relative error norm during the first few steps.

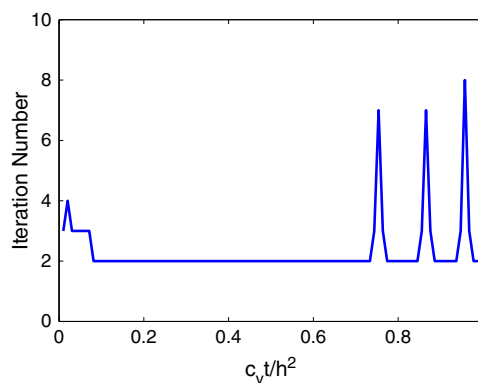


Figure 7. Iteration numbers.

which would be close to  $M_c$  for 1D problem as adopted in the benchmark case. The results also show that the more  $K_r$  is deviated from  $M_c$ , either less or greater, more iterations are needed to reach convergence, that is, slower the convergence rate.

**6.1.3. Influence of support size on convergence rate.** To investigate the influence of RKPM support size on the convergence rate, simulations are conducted using the benchmark example by assuming ( $SP = 1.02, 1.50, 1.80$ ). Note that  $SP = 1.02$  reduces RKPM interpolation similar to a conventional FEM. As shown in Figure 9, support size does not affect the number of iterations required for convergence, except for the occurrence of a few spikes in the iteration numbers. From the results it seems that support size either greater or less than  $SP = 1.50$  would initiate spikes in the iteration numbers earlier than that using  $SP = 1.50$ .

Simulations are also conducted considering different support sizes for displacement  $\mathbf{u}$  and pore fluid pressure  $p$ , denoted as  $SP_u$  for  $\mathbf{u}$  and  $SP_p$  for  $p$ , as shown in Figure 10. In general, the support size has very minor effect on the convergence rate.

**6.1.4. Stabilization at incompressible and impermeable limit.** In the proposed scheme, the displacement of solid skeleton and pore fluid pressure is approximated using the same set of nodes and the same order of interpolation. It is well known that the pore pressure distribution would exhibit nonphysical oscillation for such a case under the incompressible ( $\mathbf{S} \rightarrow 0$ ) and impermeable limit  $\mathbf{H} \rightarrow 0$ . Even though the mixture is permeable,  $\mathbf{H}\Delta t_f \rightarrow 0$  at the initial time. For all these cases, the coefficients associated with the pore pressure in fluid solver Equation (54) would vanish. As proved in the stability analysis, with properly chosen relaxation parameter, the proposed scheme is guaranteed to produce a converged solution through iterations. Here, the ‘converged’ solution sim-

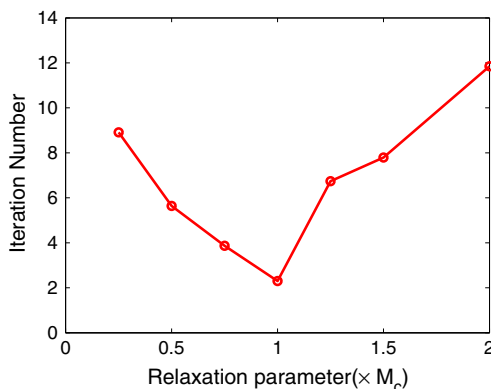


Figure 8. Different relaxation parameter.

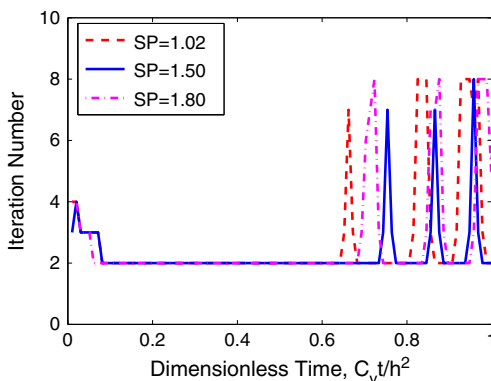


Figure 9. Different support sizes.

ply means that the solution obtained at each iteration will gradually approach a certain value as the iteration continues. The solution, however, may not converge to the real one, as can be seen from the nonstabilized oscillatory pore pressure solution shown in Figure 11 when  $c_v t/h^2$  approaches 0. Special techniques are therefore required to stabilize the pore pressure distribution at the incompressible and impermeable limit. Reference [37] proposed a streamline upwind/Petrov–Galerkin method for convection dominated flows. The method not only removes the spurious oscillation plaguing the conventional Galerkin method but also preserves the numerical accuracy. Later, [38] presented a class of Galerkin/least-square methods for advective-diffusive systems as a conceptual simplification of streamline upwind/Petrov–Galerkin, and extended the applications to a wide variety of problems. In the aforementioned development, the oscillatory solution can be numerically stabilized by adding a residual term to the Galerkin method. In this paper, the stabilization term proposed by [39] is adopted, which is based on [38].

The semi-discrete form Equation (39) can be rewritten as:

$$\begin{aligned} & \left( \int_{\Omega} \delta p_{,i} k_{ij} p_{,j} d\Omega \right)_{n+1} \Delta t_f + \left( \int_{\Omega} \delta p u_{i,i} d\Omega \right)_{n+1} - \left( \int_{\Omega} \delta p u_{i,i} d\Omega \right)_n \\ & + \left( \int_{\Omega} \delta p \frac{np}{K_f} d\Omega \right)_{n+1} - \left( \int_{\Omega} \delta p \frac{np}{K_f} d\Omega \right)_n - \left( \int_{\Gamma_p} \delta p q d\Gamma_p \right)_{n+1} \Delta t_f \quad (73) \\ & - \left( \int_{\Gamma_w} \delta p \bar{q} d\Gamma_w \right)_{n+1} \Delta t_f - \left( \int_{\Omega} \delta p_{,i} k_{ij} \rho_f b_j d\Omega \right)_{n+1} \Delta t_f = 0 \end{aligned}$$

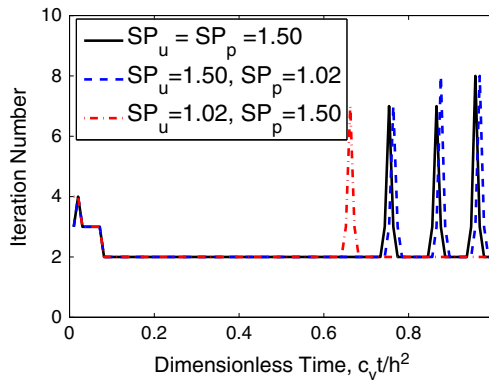


Figure 10. Different support sizes for  $u$  and  $p$ .

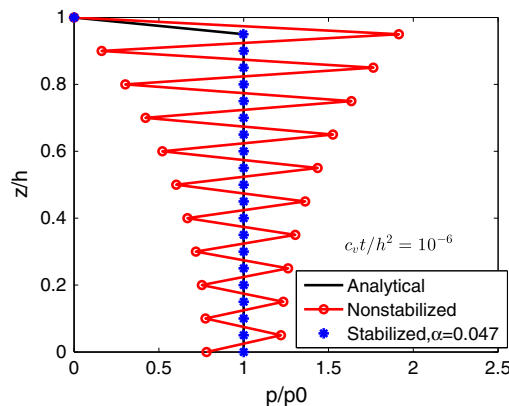


Figure 11. Stabilized  $p$  distribution at initial time.

To stabilize the pore fluid pressure distribution, the essential idea is to introduce a weighted residual term to the aforementioned fluid mass conservation equation (73) as follows:

$$\tau \cdot \int_{\Omega} \delta p_{,i} (\sigma'_{ij,j} - p_{,j} \delta_{ij} + \rho b_i) d\Omega \quad (74)$$

where  $\tau = \alpha \frac{h_c^2}{2G}$  and  $h_c$  is the characteristic length chosen as the average support size for this case.  $\alpha$  is a selected stabilization parameter. More details can be referred to [39]. The stabilized solution is shown in Figure 11. It can be seen that the method is effective in stabilizing the pore fluid pressure distribution.

## 6.2. 2D consolidation

The effectiveness of the coupled scheme is further examined through two-dimensional consolidation examples. The first example is a two-dimensional semi-infinite soil ground; the second example is a two-dimensional ground with finite depth. In these examples, the soil ground is assumed to be linearly elastic, isotropic, homogeneous and fully saturated with incompressible fluid. The pore fluid pressure generation and dissipation process and the surface settlement of examples will be compared with the analytical solutions.

**6.2.1. Consolidation in semi-infinite soil ground.** A schematic illustration of the two-dimensional (plane strain) semi-infinite ground is shown in Figure 12. On the top surface, a constant surcharge  $f$  is uniformly distributed over a width of  $2b$  during the consolidation process. Closed-form solution of the pore fluid pressure change during the consolidation has been derived in [40] and [41]. Because of symmetry of the problem, only a half part of the domain is modeled as shown in Figure 12. In this example,  $b = 0.2$  m, the height and width  $h = l = 25b = 5$  m. The height and width are chosen to be adequately large to minimize the boundary effect in order to closely approximate the infinite space. A total of  $31 \times 31$  nodes are distributed in the domain, with a denser distribution close to the footing. The surface is free draining and the remaining boundaries are impervious. For displacement boundaries, the left and right boundaries are fixed against horizontal displacement and are free in the vertical direction, while the bottom boundary is fixed against both horizontal and vertical displacement. The parameters for the material are Young's modulus  $E = 10$  MPa, Poisson's ratio  $\nu = 0$ , and hydraulic conductivity  $k_H = 5 \times 10^{-8}$  m/s. The specific weight of fluid is  $\gamma_w = 9.8$  kN/m<sup>3</sup>. To approximate incompressible fluid, the bulk modulus of fluid  $K_f$  is chosen to be  $2.2 \times 10^{20}$  Pa. A distributed load  $f = 10$  kPa is applied immediately at the start of the simulation and kept constant during the whole consolidation process. Relaxation parameter is chosen to be the same as the bulk modulus of the soil, that is,  $K_r = K = E/3(1 - 2\nu)$ . Adaptive time steps are used for the simulation. The first time step is made to obtain an adjusted time factor  $\Delta\tau = \frac{2Gk}{\gamma_w} \frac{\Delta t_f}{b^2} = 0.025$ . Later time steps would vary to shorten the simulation time. The algorithm has no difficulty in dealing with the adaptive time scale ranging from  $10^{-2}$  s to  $10^2$  s.

After loading, the pore fluid pressure build up in the whole domain. At very small adjusted time factor  $\tau$ , an approximated distribution of pore fluid pressure along the height is given in [40]. The analytical pore fluid pressure profile at location  $x/b = 0$  and at time  $\tau = 0.1$  is plotted in Figure 13 and compared with numerical results. It can be seen that the numerical results agree well with the analytical solutions. It should be noted, however, that to achieve accurate numerical results, nodal distribution should be dense enough close to the surface in order to capture the steep pore pressure change in that region. If the discretization is not fine enough, large deviation of pore pressure adjacent to the surface will be observed. Second, the simulation domain should also be sufficiently large to minimize the boundary effect. Otherwise, significant deviation of pore fluid pressure at the bottom boundary would be observed, as shown in [8].

The results of pore fluid pressure development with time at location  $x/b = 0.0, z/b = 1.0$  are also compared in Figure 14. Again, the numerical results agree very well with the analytical solutions. It is worth pointing out that the characteristic phenomenon such that the pore fluid pressure

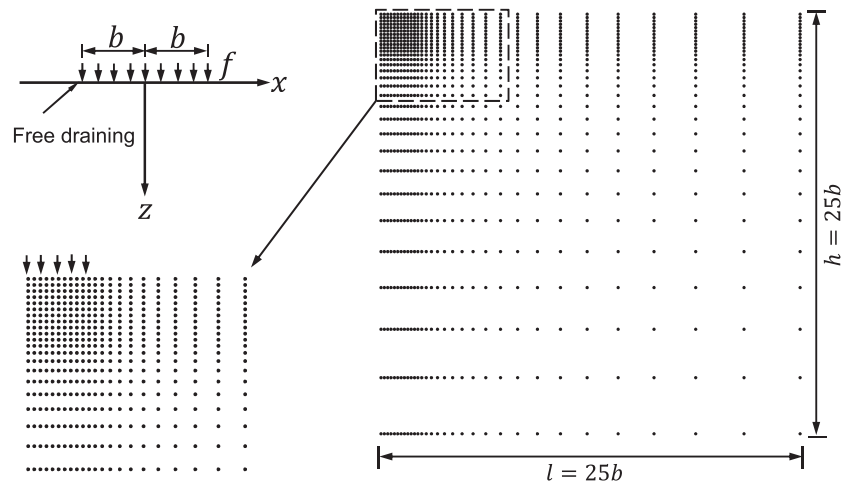


Figure 12. Model setup.

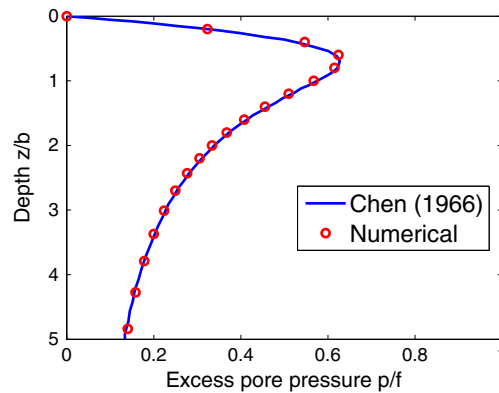


Figure 13. Pore fluid pressure profile at initial time.

increases after initial generation, known as the Mandel-Cryer effect [42, 43], can be well captured. The pore fluid pressure dissipates gradually afterwards to the end.

**6.2.2. Consolidation in a soil ground with finite depth.** The second case deals with consolidation of a finite depth of soil on a smooth rigid base under strip loading. A closed-form solution of the surface settlement has been derived by [44] and will be used for comparison in this study. The numerical model set-up is shown in Figure 15. In the numerical model,  $b = 0.2$  m, height  $h = 5b$  and width  $l = 20b$ . A total of  $21 \times 31$  nodes are distributed in the domain. The boundary conditions and material parameters are the same as the case in Section 6.2.1 except that the bottom boundary is only fixed against vertical displacement. As in the previous case, adaptive time steps are also used during the consolidation process.

Figure 16 shows the surface settlement at location  $x/b = 0, z/b = 0$  obtained by the numerical simulation and the analytical solution. Again, very close agreement is observed between the numerical and the analytical solution.

### 6.3. Biaxial test of nonlinear soil sample

A biaxial test using nonlinear soil model is also conducted to test the applicability of the developed scheme in fully nonlinear simulations. The model set-up is shown in Figure 17. The sample is of size  $5 \text{ cm} \times 10 \text{ cm}$ .  $11 \times 21$  nodes are evenly distributed in the domain for spatial discretization with a support size  $SP = 1.8$ . A constant confining pressure of  $\sigma_h = 2 \text{ MPa}$  is applied on the sample.

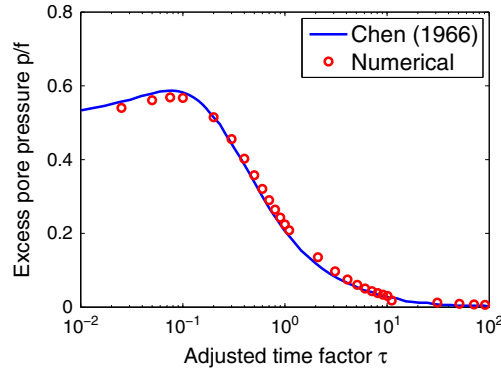


Figure 14. Pore fluid pressure development with time.

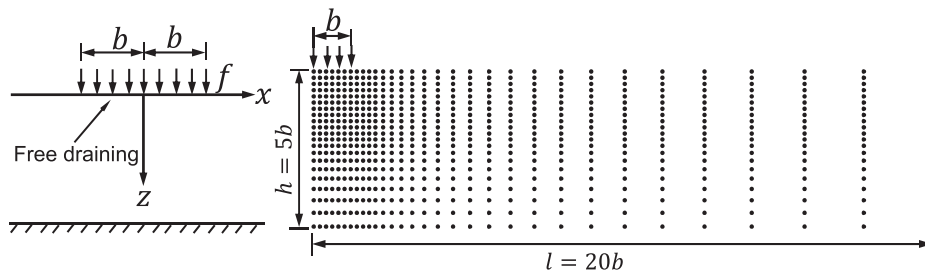


Figure 15. Model setup for finite depth consolidation.

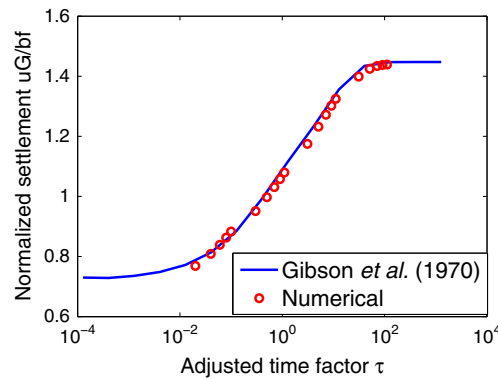


Figure 16. Surface settlement at  $x/b = 0, z/b = 0$ .

The bottom nodes are fixed while the top nodes are loaded using displacement control, and all the boundaries are impermeable. A fully nonlinear soil model, the bounding surface hypo-plasticity model [45], is used to model the soil behavior. The soil parameters are tabulated in Table II, which correspond to typical values for loose sands with an initial void ratio 0.88. In the table,  $M, e_{\Gamma}, \lambda_c$  and  $\xi$  are parameters related to the critical state of the soils.  $m$  and  $n$  are parameters to describe the so-called phase-transformation state, where the volumetric behaviors of the soil change from dilation to contraction.  $G_0$  and Poisson's ratio  $\nu$  are used to calculate nonlinear elastic shear and bulk moduli, while  $h_r$  is related to plastic shear modulus.  $k_r, a$  and  $b$  are parameters for the plastic bulk modulus at monotonic loading stage, while  $d$  is used for the plastic bulk modulus in an unloading/reloading stage. Interested readers may refer to [45–47] for the detailed explanation of the bounding surface model and related parameters.

Figure 18(a) shows the contour of equivalent strain at an axial strain of 5.2%. Two conjugate shear bands clearly demonstrate the strain localization behavior of the soil under undrained shearing. The

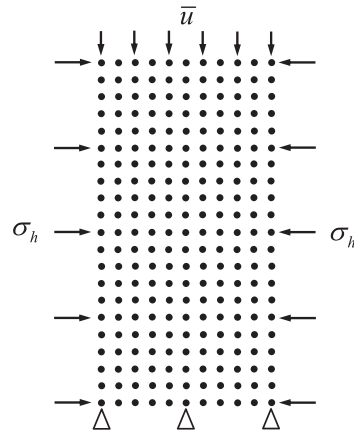


Figure 17. Biaxial model set-up.

Table II. Parameters for bounding surface hypo-plasticity model.

Critical state	Phase transformation	Elastic moduli	Plastic shear modulus	Plastic bulk modulus
$e_{\Gamma} = 0.934$	$m = 3.5$	$G_0 = 200$	$h_r = 0.13$	$k_r = 0.65$
$\lambda_c = 0.019$	$n = 0.75$	$\nu = 0.05$		$a = 0$
$\xi = 0.7$				$b = 1.5$
$M = 1.25$				$d = 2.2$

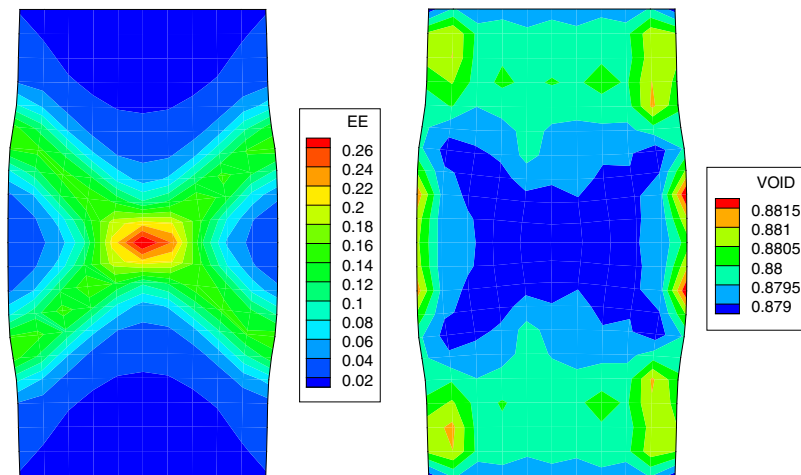


Figure 18. (a) Contour of equivalent strain. (b) Contour of void ratio.

void ratio is redistributed to exhibit a similar pattern as that of the equivalent strain, as is shown in Figure 18(b). Within the shear band, the loose sand is extensively sheared and become more contractive. Therefore smaller void ratio is observed within the shear band. There are also small zones where the void ratio is greater than the initial void ratio. These zones correspond to the dilative region where the soil sample is bulging out. This example clearly demonstrates the applicability of the developed scheme in simulating fully coupled nonlinear soil behaviors.

## 7. CONCLUSIONS

In this paper, the coupled hydro-mechanical system is formulated in the weak form using RKPM for spatial discretization. The primary unknowns, the displacement of solid–fluid mixture and pore fluid pressure, are modeled using the same set of nodes and equal order of interpolation. An iterative coupling scheme is developed to solve the solid and fluid system sequentially and iteratively.

Without stabilization, the iterative scheme is only conditionally stable. Using a simple stabilization term, the algorithm is proved to be unconditionally stable. The relaxation parameter  $K_r$  can greatly affect the convergence rate, so it should be properly chosen to accelerate the iterations and reduce the computational cost. Through limited numerical simulations, it is recommended that  $K_r$  should equal to the constrained or unconstrained bulk modulus of the soil for 1D and 2D/3D simulation. On the other hand, the RKPM support size has little effect on the convergence rate. At the impermeable and undrained limit, additional stabilization is needed to eliminate the pressure oscillation.

The numerical performance of the algorithm is demonstrated through one-dimensional and two-dimensional consolidation examples. Using a fully nonlinear soil model, the model can also well capture the complicated soil-behavior and pore-pressure generation during biaxial loading, showing its great promise for use in solving practical problems.

## ACKNOWLEDGEMENTS

Financial support from Research Project Competition (UGC/HKUST) grant No. RPC11EG27 and Hong Kong Research Grants Council RGC 620311 is gratefully acknowledged.

## REFERENCES

- Zienkiewicz O, Chan A, Pastor M, Schrefler B, Shiomi T. *Computational Geomechanics with Special Reference to Earthquake Engineering*. John Wiley: Chichester and New York, 1999.
- Modaressi H, Aubert P. Element-free Galerkin method for deforming multiphase porous media. *International Journal for Numerical Methods in Engineering* 1998; **42**(2):313–340.
- Oliaei M, Soga K, Pak A. Some numerical issues using element-free Galerkin mesh-less method for coupled hydro-mechanical problems. *International Journal for Numerical and Analytical Methods in Geomechanics* 2009; **33**: 915–938.
- Hua L. Stable element-free Galerkin solution procedures for the coupled soil–pore fluid problem. *International Journal for Numerical Methods in Engineering* 2011; **86**:1000–1026.
- Karim M, Nogami T, Wang J. Analysis of transient response of saturated porous elastic soil under cyclic loading using element-free Galerkin method. *International Journal of Solids and Structures* 2002; **39**:6011–6033.
- Murakami A, Kawabata H, Aoyama S. EFGM analysis for saturated soil. *Computer Methods and Advances in Geomechanics* 2000; **1**:153–156.
- Samimi S, Pak A. Three-dimensional simulation of fully coupled hydro-mechanical behavior of saturated porous media using element free Galerkin (EFG) method. *Computers and Geotechnics* 2012; **46**:75–83.
- Khoshghalb A, Khalili N. A stable meshfree method for fully coupled flow-deformation analysis of saturated porous media. *Computers and Geotechnics* 2010; **37**:789–795.
- Soares D. Iterative dynamic analysis of linear and nonlinear fully saturated porous media considering edge-based smoothed meshfree techniques. *Computer Methods in Applied Mechanics and Engineering* 2013; **253**:73–88.
- Wang J, Liu G, Lin P. Numerical analysis of Biot's consolidation process by radial point interpolation method. *International Journal of Solids and Structures* 2002; **39**:1557–1573.
- Wang J, Liu G, Wu Y. A point interpolation method for simulating dissipation process of consolidation. *Computer Methods in Applied Mechanics and Engineering* 2001; **190**(45):5907–5922.
- Bui HH, Fukagawa R, Sako K, Ohno S. Lagrangian meshfree particles method (SPH) for large deformation and failure flows of geomaterial using elastic–plastic soil constitutive model. *International Journal for Numerical and Analytical Methods in Geomechanics* 2008; **32**:1537–1570.
- O'Sullivan C, Bray JD, Li S. A new approach for calculating strain for particulate media. *International Journal for Numerical and Analytical Methods in Geomechanics* 2003; **27**(10):859–877.
- Li S, Hao W, Liu WK. Mesh-free simulations of shear banding in large deformation. *International Journal of Solids and Structures* 2000; **37**(48):7185–7206.
- Li S, Liu WK. Reproducing kernel hierarchical partition of unity, part II: Applications. *International Journal for Numerical Methods in Engineering* 1999; **45**(3):289–317.
- Li S, Liu WK. Numerical simulations of strain localization in inelastic solids using mesh-free methods. *International Journal for Numerical Methods in Engineering* 2000; **48**(9):1285–1309.

17. Liu W, Jun S, Zhang YF. Reproducing kernel particle methods. *International Journal for Numerical Methods in Fluids* 1995; **20**:1081–1106.
18. Shibata T, Murakami A. A stabilization procedure for soil-water coupled problems using the element-free Galerkin method. *Computers and Geotechnics* 2011; **38**(5):585–597.
19. Kim J. Sequential methods for coupled geomechanics and multiphase flow. *Ph.D. Thesis*, Stanford University, 2010.
20. Settari A, Walters D. Advances in coupled geomechanical and reservoir modeling with applications to reservoir compaction. *SPE Journal, Society of Petroleum Engineers* 2001; **6**(3):334–342.
21. Joosten M, Dettmer W, Perić D. Analysis of the block Gauss–Seidel solution procedure for a strongly coupled model problem with reference to fluid–structure interaction. *International Journal for Numerical Methods in Engineering* 2009; **78**(7):757–778.
22. Whiteley J, Gillow K, Tavener S, Walter A. Error bounds on block Gauss–Seidel solutions of coupled multiphysics problems. *International Journal for Numerical Methods in Engineering* 2011; **88**(12):1219–1237.
23. Ehlers W, Zinatbakhsh S, Markert B. Stability analysis of finite difference schemes revisited: A study of decoupled solution strategies for coupled multifield problems. *International Journal for Numerical Methods in Engineering* 2013; **94**(8):758–786.
24. Kim J, Tchelepi H, Juanes R. Stability and convergence of sequential methods for coupled flow and geomechanics: Drained and undrained splits. *Computer Methods in Applied Mechanics and Engineering* 2011a; **200**(23):2094–2116.
25. Kim J, Tchelepi H, Juanes R. Stability and convergence of sequential methods for coupled flow and geomechanics: Fixed-stress and fixed-strain splits. *Computer Methods in Applied Mechanics and Engineering* 2011b; **200**(13):1591–1606.
26. Murakami A, Setsuyasu T, Arimoto S-I. Mesh-free method for soil-water coupled problem within finite strain and its numerical validity. *Soils and Foundations* 2005; **45**(2):145–154.
27. Wang Z-L, Li Y-C. Analysis of factors influencing the solution of the consolidation problem by using an element-free Galerkin method. *Computers and Geosciences* 2006; **32**(5):624–631.
28. Wang J, Zhang B, Nogami T. Wave-induced seabed response analysis by radial point interpolation meshless method. *Ocean Engineering* 2004; **31**(1):21–42.
29. Liu WK, Li S, Belytschko T. Moving least-square reproducing kernel methods (I) methodology and convergence. *Computer Methods in Applied Mechanics and Engineering* 1997; **143**(1):113–154.
30. Chen J-S, Pan C, Wu C.-T. Large deformation analysis of rubber based on a reproducing kernel particle method. *Computational Mechanics* 1997; **19**:211–227.
31. Li S, Liu W. Meshfree and particle methods and their applications. *Applied Mechanics Reviews* 2002; **55**:1–34.
32. Li S, Liu WK. *Meshfree Particle Methods*. Springer-Verlag: Berlin Heidelberg, 2004.
33. Jun S, Liu W, Belytschko T. Explicit reproducing kernel particle methods for large deformation problems. *International Journal for Numerical Methods in Engineering* 1998; **41**:137–166.
34. Belytschko T, Liu WK, Moran B. *Nonlinear Finite Element Analysis for Continua and Structures*, Vol. 1. Wiley, 2000.
35. Turska E, Wisniewski K, Schrefler B. Error propagation of staggered solution procedures for transient problems. *Computer Methods in Applied Mechanics and Engineering* 1994; **114**(1):177–188.
36. Verruijt A, van Baars S. *Soil Mechanics*. VSSD: Delft, The Netherlands, 2012.
37. Brooks AN, Hughes TJ. Streamline upwind/Petrov-Galerkin formulations for convection dominated flows with particular emphasis on the incompressible Navier-Stokes equations. *Computer Methods in Applied Mechanics and Engineering* 1982; **32**(1):199–259.
38. Hughes TJ, Franca LP, Hulbert GM. A new finite element formulation for computational fluid dynamics: VIII. The Galerkin/Least-squares method for advective-diffusive equations. *Computer Methods in Applied Mechanics and Engineering* 1989; **73**(2):173–189.
39. Wan J. Stabilized finite element methods for coupled geomechanics and multiphase flow. *Ph.D. Thesis*, Stanford University, 2002.
40. Chen AT. Plane strain and axisymmetric primary consolidation of saturated clays. *Ph.D. Thesis*, Rensselaer Polytechnic Institute, 1966.
41. Schiffman RL, Chen AT, Jordan JC. An analysis of consolidation theories. *Journal of Soil Mechanics and Foundations Division* 1969; **95**:285–312.
42. Cryer CW. A comparison of the three-dimensional consolidation theories of Biot and Terzaghi. *The Quarterly Journal of Mechanics and Applied Mathematics* 1963; **16**(4):401–412.
43. Mandel J. Consolidation Des Sols (étude Mathématique). *Géotechnique* 1953; **3**(7):287–299.
44. Gibson R, Schiffman R, Pu S. Plane strain and axially symmetric consolidation of a clay layer on a smooth impervious base. *The Quarterly Journal of Mechanics and Applied Mathematics* 1970; **23**(4):505–520.
45. Li X, Dafalias Y, Wang Z. State-dependent dilatancy in critical-state constitutive modelling of sand. *Canadian Geotechnical Journal* 1999; **36**:599–611.
46. Wang G, Xie Y. Modified bounding surface hypoplasticity model for sands under cyclic loading. *Journal of Engineering Mechanics* 2014; **140**(1):91–101.
47. Wang Z, Dafalias Y, Shen C. Bounding surface hypoplasticity model for sand. *Journal of Engineering Mechanics* 1990; **116**(5):983–1001.